



Eruption chronologies, plume heights and eruption styles at Tungurahua Volcano: Integrating remote sensing techniques and infrasound

Andrea M. Steffke^{a,*}, David Fee^b, Milton Garces^b, Andrew Harris^c

^a *Hawai'i Institute of Geophysics and Planetology, School of Ocean and Earth Science and Technology, University of Hawaii at Manoa, 1680 East-West Road, Honolulu, HI 96822, USA*

^b *Infrasound Laboratory, University of Hawaii at Manoa, 73-4460 Queen Kaahumanu Hwy, #119, Kailua Kona, HI 96740, USA*

^c *Laboratoire Magmas et Volcans, Université Blaise Pascal, 5 Rue Kessler, 63038, Clermont-Ferrand, France*

ARTICLE INFO

Article history:

Received 18 November 2009

Accepted 15 March 2010

Available online 27 March 2010

Keywords:

remote sensing
volcanic plumes
infrasound
Tungurahua
ash monitoring

ABSTRACT

Satellite remote sensing allows volcanic ash plumes to be detected and tracked and routinely aids in hazard mitigation, especially to the aviation community. Although satellite imagery provides valuable information about volcanic plume processes (i.e. plume heights, plume composition and plume transport), it has its limitations. In addition to the observational gaps produced by meteorological clouds as well as temporal and spatial resolution restrictions, large volcanic clouds often obscure the vent during an eruption. Therefore, some key information about eruption dynamics and processes are impossible to obtain from satellite images. In this paper we investigate four eruptions at Tungurahua Volcano, Ecuador during the 2006–2008 time period. We integrate satellite-derived eruption chronologies, plume heights and plume aspect ratios with infrasound data, primarily acoustic power and hand-held thermal imagery when available. Integrating these datasets allows us to identify accurate eruption onsets, durations and cessations as well as define different types of eruption styles ranging from plinian to weak vulcanian. Transitions between the different eruption styles were also documented. Results show that there is a positive correlation between plume height and acoustic power. We conclude that combining the two datasets allows better constraints on eruption processes and source parameters. Using these methods in real-time monitoring will allow more accurate eruption monitoring and ash hazard mitigation.

© 2010 Elsevier B.V. All rights reserved.

1. Introduction

Explosive volcanic eruptions produce ash plumes and pyroclastic flows that create hazards to surrounding communities. In addition, volcanic plumes pose a threat to the aviation community and can affect air traffic routes hundreds of kilometers away from the volcano (Casadevall et al., 1992; Rose et al., 1995; Casadevall and Krohn, 1995; Dean et al., 2004). Effective monitoring of these plumes is difficult due to the dangerous nature of explosive eruptions, often remote location of volcanoes, and the inability to view large eruption plume dispersal patterns from the ground. The synoptic view of satellites allow for the detection of volcanic plumes irrespective of light conditions and the opportunity to detect changes in the transport and dispersion of a plume as it traverses the globe (Matson, 1984). Without the use of satellite data, eruption plume dispersal could not be accurately monitored. Satellite remote sensing techniques are routinely used to identify and track these plumes and thereby aid in hazard management (e.g. Kienle and Shaw, 1979; Holasek and Self, 1995; Holasek et al., 1996a; Schneider

et al., 1999). Integrating satellite data with other observations of eruptions producing volcanic plumes (e.g., visual observations, ground-based thermal imagery, radar, seismic and infrasound data) enables different eruption regimes to be better identified and classified, thereby enhancing monitoring efforts.

The purpose of this research is to use Geostationary Operational Environmental Satellite (GOES) and Moderate Resolution Imaging Spectroradiometer (MODIS) satellite data to develop eruption chronologies, determine eruption dynamics, and estimated ash plume ceilings during different eruption regimes at Tungurahua Volcano, Ecuador, during the 2006–2008 study period. This paper will expand on the previous investigation of monitoring efforts using infrasound and satellite data at Tungurahua (Garces et al., 2008) and incorporate the infrasound observations presented in a companion paper of Fee et al. (in press). Both data types allow remote monitoring of volcanic activity at different temporal and spatial resolutions, and their synergy enables both continuous near-vent overpressure (infrasound) and ash plume dispersal (satellite) process to be quantified. The integration of infrasound data as well as visual observations and thermal camera imagery enables us to constrain: (1) what types of eruptions can be identified using satellite data and (2) what changes in eruption mechanisms can be inferred using satellite imagery, infrasound data, and ground-based thermal imagery.

* Corresponding author. Tel.: +1 808 956 0182; fax: +1 808 956 6322.

E-mail addresses: steffke@higp.hawaii.edu (A.M. Steffke), dfee@isla.hawaii.edu (D. Fee), milton@isla.hawaii.edu (M. Garces), A.Harris@opgc.univ-bpclermont.fr (A. Harris).

2. Background

2.1. Tungurahua Volcano

Tungurahua Volcano (1.476 S, 78.442 W) is located in Ecuador approximately 140 km south of the capital city of Quito (Fig. 1). The 5023 m andesite–dacite stratovolcano is considered one of the most active volcanoes in Ecuador (BGVN, 2008). Tungurahua is composed of three major volcanic edifices constructed in the mid-Pleistocene. The active cone (Tungurahua III) is located inside a large horse-shoe shaped caldera (Fig. 1) that formed during a large debris avalanche ~3000 years ago (Hall et al., 1999). All historic volcanic activity has occurred at the summit vent and has been generally characterized by strombolian to vulcanian explosions, occasionally accompanied by pyroclastic flows, lava flows and lahars that have inundated populated areas surrounding the flanks of the volcano (BGVN, 2008). Although there was a hiatus in the historic eruptive activity from 1918 to 1999, since 1999 eruptive activity has resumed and is characterized by vulcanian activity and associated convective plumes from the central vent (Johnson, 2003; Arellano et al., 2008; BGVN, 2008). During the 2002–2008 period the volcano has experienced several alternating periods of increased activity, with the most energetic periods starting in the spring of 2006 and continuing today (Arellano et al., 2008).

2.2. Satellite data

A variety of satellite sensors are used to detect volcanic plumes including the Advanced Very High Resolution Radiometer (AVHRR) (Wen and Rose, 1994; Holasek et al., 1996a), Total Ozone Mapping Spectrometer (TOMS) (Krueger, 1982; Robock and Matson, 1983), GOES (Glaze et al., 1989; Dean et al., 2004) and MODIS (Dean et al., 2004; Watson et al., 2004). Image selection depends on the desired time period, temporal and spatial resolutions, location, and properties of the plume. For this project the GOES Imager and MODIS sensors were utilized to gather temperature and velocity measurements of the plumes erupted at Tungurahua. GOES data was used to determine an eruption chronology and plume heights at a high temporal resolution while MODIS data were used, when available, for more spatially robust observation of the plumes.

The GOES Imager is carried on the NOAA GOES geostationary satellite. Because the satellite is located at a high altitude (35,786 km) it is able to acquire images at a high temporal resolution by sweeping the entire earth disk at a high temporal frequency, thus trading spatial resolution for increased field of view and temporal resolution. The sensor acquires images of South America once every 30 min and collects data in five spectral bands. These bands are located in the visible (Band 1: 0.6 μm), mid-infrared (Band 2: 3.9 μm), water vapor

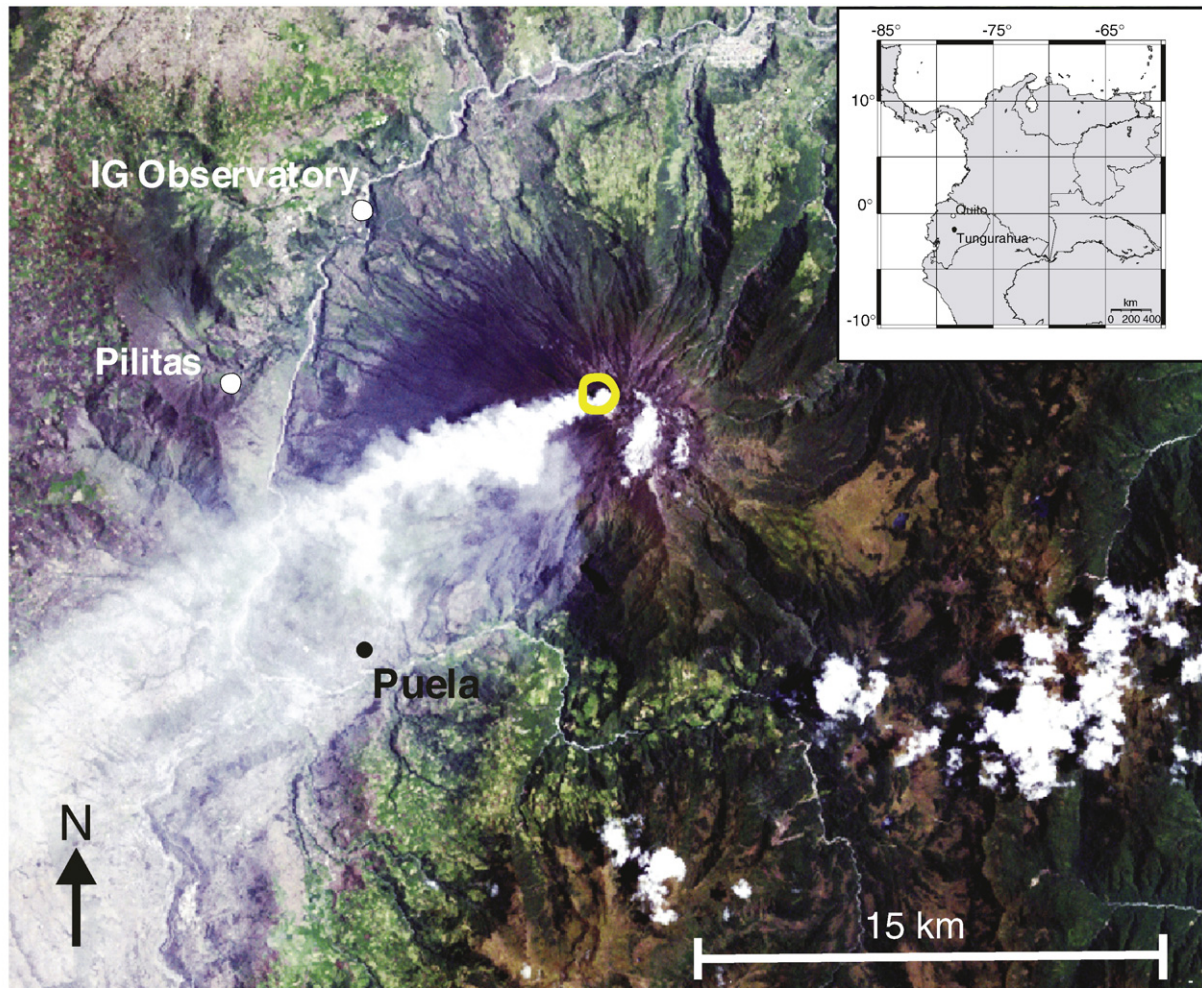


Fig. 1. Location map of Tungurahua Volcano. Map showing location of Tungurahua in Ecuador (inset) and a Landsat ETM+ image (1/28/2004) showing location of Tungurahua, summit crater (yellow circle) and IG observatory.

infrared band (Band 3: 6.7 μm), thermal infrared band (Band 4: 10.7 μm) and CO_2 absorption band (Band 13.3 μm). For this study GOES Band 1, with a spatial resolution of 1.0 km^2 and Band 4, with a spatial resolution of 4.0 km^2 were used to identify volcanic clouds and estimate their heights.

Unlike GOES, the MODIS sensor is flown on NASA's polar orbiting satellites Aqua and Terra and therefore collects data at a lower temporal resolution. Each satellite makes equatorial crossings twice daily limiting the number of observations to two images per sensor, per day. Optimally, a total of four images can be used for plume monitoring daily. The MODIS sensors collect data in 36 spectral bands, but only five were used to identify volcanic plumes in this study. There were visible bands 1 (0.62–0.67 μm), 2 (0.841–0.876 μm), 3 (0.459–0.479 μm), and 4 (0.545–0.565 μm), and TIR bands 31 (10.78–11.28 μm) and 32 (11.77–12.27 μm). Bands 1 and 2 have a spatial resolution of 0.25 km^2 at nadir, and bands 3 and 4 have a spatial resolution of 0.5 km^2 at nadir. Since half of the images were acquired at night VIS imagery could only be used during the day. The TIR bands have a spatial resolution of 1 km^2 at nadir. The visible bands were chosen because they have the highest spatial resolution, allowing for the most detailed observations within the individual plumes. Bands 31 and 32 were used because they are located within the atmospheric window in the TIR, allowing temperatures of the plumes to be calculated, and thus heights estimated.

2.3. Remote sensing techniques for determining plume heights

Various techniques can be used to estimate volcanic plume heights (See Sparks et al., 1997 for a review). Two of the more widely accepted forms are used in this study: velocity determination and plume top temperature (PTT).

The first (velocity determination) method uses plume velocities obtained from a time-series of satellite imagery. These data are used to track the relative movement of the plume over a specified period of time to obtain plume height. The method involves first obtaining the direction of plume movement from a group of images acquired closely spaced in time, and the distance the plume has moved over a given time step (to obtain the velocity). Comparing these measurements with wind field data for the area allows plume heights to be constrained by determining the height at which the wind speed and direction required to transport the plume at the measured velocities and vectors (Sparks et al., 1997). Since wind speeds and vectors can be comparable at different elevations it can be difficult to make precise height estimates of the plumes, and there can be an uncertainty range of several hundred to thousands of meters in plume height estimates. The National Centers for Environmental Prediction (NCEP) Global Data Assimilation System (GDAS) global wind field data and the Naval Research Laboratory (NRL) Ground to Space (G2S) atmospheric specifications were compared to one another. Although both products are global datasets with a spatial resolution of 1° latitude and longitude, the G2S data is produced by fusing empirical models with Numerical Weather Prediction specifications and yields global atmospheric specifications that are seamless up to the upper atmosphere (Drob et al., 2003). Therefore the G2S profiles have a higher, more accurate vertical grid spacing and have been utilized in this chapter whenever available. The profiles provide numerous atmospheric parameters for a given height and latitude/longitude, such as temperature, wind speed, wind direction, and atmospheric pressure. For this study we were only interested in atmospheric elevation and its associated wind speed, wind direction and temperature.

The second (PTT) method uses TIR satellite data that is converted to temperatures and then used to determine the temperature of the plume top. As a volcanic plume rises it entrains large amounts of air and cools rapidly. If one assumes that the coldest plume top temperature relates to the portion of that plume that has cooled to

the surrounding atmospheric temperature one can then compare plume temperature with that of the atmospheric profiles for the region to constrain the height. For this technique it is important to only measure the temperature of opaque plumes, so that there is no contributing radiation from the underlying ground (Sparks et al., 1997). Radiosonde data were not available for all days of the eruptions and the closest location of the balloon launch was over 500 km away. Therefore G2S and GDAS atmospheric profiles were used alongside the minimum temperatures calculated from the TIR satellite data and then correlated those temperatures with the atmospheric temperatures to estimate the plume heights. The elevations with the closest temperature (below and above) as the minimum plume temperatures recorded are estimated to be the maximum and minimum plume heights.

2.4. Infrasound data

Infrasound data are also utilized to help constrain and characterize vent processes during the eruptions. A four element array, RIOE, located ~36.75 km southwest of Tungurahua volcano collected data during the eruption periods. Chaparral 2.2a microphones, with a flat frequency response between 0.1 and 200 Hz, were deployed in as 4-element arrays and sampled at 40 Hz. Volcanic signals were detected using the Progressive Multi-Channel Correlation (PMCC) array processing method (Cansi, 1995). A variety of processing techniques are used for characterizing volcanic eruption signals that may be associated with ash ejection, but in this manuscript we primarily use acoustic power levels associated with jetting events. Acoustic power was determined by averaging the acoustic energy over a 15 minute window. The acoustic power was used because it appears to be the best indicator of significant changes in volume flux at the volcano (Fee et al., in press). The sound power levels were related to the satellite observations to detect changes in mass flux.

3. Eruption chronology and volcanic plume heights

Four eruptions of Tungurahua are investigated in this study: The 10–11 January 2008, 6 February 2008, 14–15 July 2006, and the 16–17 August 2006 eruptions. These eruptions were chosen based on the features of the infrasound signals, the amount of cloud-free satellite data available, existing hand-held thermal imagery, and visual observations. The eruptions are described in order of increasing intensity based upon the maximum observed plume heights and the amount of recorded acoustic energy. The satellite chronology and plume heights for each of these eruptions are given in Tables 1a, 1b–4. All times and dates discussed in the section refer to UTC and all plume heights are elevation above sea level (a.s.l.).

3.1. January 10th–11th eruption

On January 10th 2008 10:45, GOES TIR detected a narrow plume (8 km wide) extending 8 km east of Tungurahua (Fig. 2a). Prior to this time, no plumes were observed. Throughout the next 4 h the images display the plume attached to the summit and extended a maximum distance of 22 km. Meteorological clouds started to accumulate over the volcano at 14:15 obscuring the satellites view of the plume; therefore it was not possible to determine when the eruption ended.

The plume velocities and temperatures calculated using GOES TIR data (Table 1a) were compared with the GDAS atmospheric profiles for the region. Comparing the velocity and temperature measurements with the wind profiles place the plume between 5000 and 6650 m (Table 1a).

Two small eruptions occurred on January 11th 2008. The first clear view of the volcano occurred at 03:15; GOES TIR data shows a plume extending 16 km north of Tungurahua. From 03:45 to 06:45 the plume continued to travel to the northwest and did not grow much in

Table 1a

January 10th 2008 eruption plume temperatures, velocities and estimated plume top heights as well as additional comments about plumes dispersal patterns.

Date/time (UTC)	Min temp (°C)	Min height (m)	Max height (m)	Velocity (m s ⁻¹)	Min height (m)	Max height (m)	Comments
1/10/08 10:45	-3	5100	5850	0.0	5850	6650	Thin continuous plume extending east of the volcano
1/10/08 11:15	-2	5100	5850	1.7	5850	6650	
1/10/08 11:45	-2	5100	5850	2.2	5850	6650	
1/10/08 12:15	-1	4400	5100	0.0	5850	6650	
1/10/08 12:45	2	4400	5100	2.2	5850	6650	
1/10/08 13:15	-1	4400	5100	2.8	5850	6650	

Table 1b

11 January 2008 eruption plume temperatures, velocities and estimated plume top heights as well as additional comments about plumes dispersal patterns.

Date/time (UTC)	Min temp (°C)	Min height (m)	Max height (m)	Velocity (m s ⁻¹)	Min height (m)	Max height (m)	Comments
1/11/08 03:15	-4	5100	5850		5100	5850	Small plume extending north of volcano
1/11/08 03:45	-4	5100	5850	2.2	5100	5850	
1/11/08 04:15	-4	5100	5850	6.7	5100	5850	Plume's direction changes to northwest
1/11/08 04:45	-5	5850	6650	2.2	5100	5850	
1/11/08 05:15	-5	5850	6650	6.7	5100	5850	
1/11/08 05:45	-4	5100	5850	8.3	5100	5850	
1/11/08 06:15	-4	5100	5850	1.1	5100	5850	
1/11/08 06:45	-5	5850	6650		5100	5850	
1/11/08 11:45				0.0	5850	7550	Small plume traveling to the west
1/11/08 12:15				2.2	5850	7550	
1/11/08 12:45				2.2	5850	7550	
1/11/08 13:15				1.7	5850	7550	New plume observed extending to the northwest. Older plume detached from summit
1/11/08 13:45				0.0	5850	7550	
1/11/08 14:15				0.0	5850	7550	
1/11/08 14:45				0.6	5850	7550	
1/11/08 15:15				1.1	5850	7550	
1/11/08 15:45				1.7	5850	7550	
1/11/08 16:15				2.2	5850	7550	
1/11/08 16:45				2.2	5850	7550	
1/11/08 17:15				0.0	5850	7550	

length and reached a maximum distance of 28 km from the volcano (Fig. 2b). Although clear conditions occurred after 06:45 no plumes were observed at Tungurahua until 11:15 the same day. A second eruption was observed at 11:15 (Fig. 2c). The eruption was not identifiable in the TIR imagery but since this eruption occurred during the day, visible imagery were utilized to gather length and width measurements. Between 11:45 and 17:15 one continuous plume was emitted north of the volcano reaching a maximum distance of 33 km

from the vent (Fig. 2c and d). After 17:15 the plume becomes difficult to distinguish from the surrounding meteorological clouds (Fig. 2d).

The velocities gathered from the satellite data show similar trends to the January 10th eruption (Table 1a). Comparing the velocities to the GDAS data suggests the first plume altitude was between 5100 and 5850 m (Table 1b). The velocities and temperatures of the second eruption plume suggest the plume reached altitudes between 5100 and 7550 m (Table 1b).

Table 2

February 6th 2008 eruption plume temperatures, velocities and estimated plume top heights as well as additional comments about plumes dispersal patterns.

Phase	Date/time (UTC)	Min temp (°C)	Min height (m)	Max height (m)	Velocity (m s ⁻¹)	Min height (m)	Max height (m)	Comments
1	2/6/2008 04:45	-6	6000	6600	3.9	6000	6600	Plume One observed at summit
	2/6/2008 05:15	-4	5450	6000	6.7	6000	6600	Plume One detaches from summit
2	2/6/2008 05:45	-18	7800	8400	8.6	6000	6600	Plume Two observed at summit
	2/6/2008 06:15	-23	8400	8900	8.8	6000	6600	Plume Two increases in length and width
	2/6/2008 06:45	-23	8400	8900	5.9	6000	6600	
	2/6/2008 07:15	-21	7800	8400	9.3	6000	6600	Leading edge of Plume Two moves to the southwest
	2/6/2008 07:45	-18	7800	8400	9.8	8400	8900	Plume Two starting to separate forming an eruption cloud and plume still attached to summit.
	2/6/2008 08:15	-16	7200	7800	5.9	8400	8900	Leading edge of Plume Two moves to the southwest
	2/6/2008 08:45							Meteorological clouds obscure view
	2/6/2008 09:15							Meteorological clouds obscure view
3	2/6/2008 09:45	-8	6600	7200	2.8	7200	7800	Plume Three observed at summit
	2/6/2008 10:15	-22	8400	8900	10.0	10,500	10,900	Plume Three increases in length and width
	2/6/2008 10:45	-21	7800	8400	7.1	10,500	10,900	
4	2/6/2008 11:15	-19	7800	8400	8.3	10,500	10,900	Plume Three is decreases in width near summit region
	2/6/2008 11:45	-17	7800	8400	7.1	10,500	10,900	Plume Three increases in length and width
	2/6/2008 12:15	-11	6600	7200			14,300	Leading edge of plume not in image.
	2/6/2008 12:45	-16	7200	7800			14,300	Max velocity determined heights taken from VAAC report
	2/6/2008 13:15	-17	7800	8400			14,300	
	2/6/2008 13:45	-16	7200	7800			14,300	
	2/6/2008 14:15	-20	7800	8400			14,300	

Table 3

July 14th–15th 2006 eruption plume temperatures, velocities and estimated plume top heights as well as additional comments about the plume's dispersal patterns.

Phase	Date/time (UTC)	Min temp (°C)	Min height (m)	Max height (m)	Velocity (m s ⁻¹)	Min height (m)	Max height (m)	Comments
1	7/14/06 22:45	-6	6000	6250	2.2	6000	6250	Plume first observed in TIR. Thin plume extending to the west of the vent.
	7/14/06 23:15	-31	9750	10,000	10.0	6000	6250	Plume increases in width and length.
	7/14/06 23:45	-46	11,500	11,750	7.2	13,250	13,500	
2	7/15/06 0:15	-55	12,500	12,750	8.2	13,250	13,500	Large increase in plumes intensity. Plume being dispersed to the west and southwest.
	7/15/06 0:45	-66	14,000	14,250	16.7	13,250	13,500	
	7/15/06 01:15	-67	14,250	14,500	12.6	13,750	14,000	Western component of the plume not as prominent. Principle direction of transport is to the southwest.
	7/15/06 01:45	-68	14,500	14,750	12.2	14,000	14,250	Plume being transported to the southwest.
	7/15/06 02:15	-65	14,000	14,250	13.3	14,000	14,250	
3	7/15/06 02:45	-59	13,000	13,250	13.3	14,000	14,250	
	7/15/06 03:15	-56	12,750	13,000	11.1	14,000	14,250	Eruption cloud has drifted to the southwest allowing vent to be observed. Plume still attached to summit.
	7/15/06 03:45	-53	12,250	12,500	15.0	14,000	14,250	Large eruption cloud still being dispersed to the southwest.
	7/15/06 04:15	-37	10,500	10,750	7.2	14,000	14,250	Large eruption cloud still being dispersed to the southwest.
	7/15/06 04:45	-27	9250	9500	7.2	14,000	14,250	Large eruption clouds leading edge is difficult to discern therefore the velocity and temperatures cannot be accurately measured. Summit temperatures and estimated heights. Velocity measurements could not be made because leading edge of plume still under eruption cloud.
	7/15/06 03:45	-16	7750	8000				Plume still attached to the vent.
	7/15/06 04:15	-10	6750	7000				Plume still attached to the vent.
	7/15/06 05:15	-10	6750	7000				
	7/15/06 05:45	-11	6750	7000				
	7/15/06 06:15	-11	6750	7000				
	7/15/06 06:45	-14	7500	7750				
7/15/06 07:15	-11	6750	7000					

3.2. February 6th 2008 eruption

The eruption of February 6th 2008 was characterized by four different explosive events, each producing separate volcanic plumes. Phase One began when GOES band 4 imagery first detected a 4 km wide plume (Plume One) extending 8 km south at 04:45 (Fig. 3a). In the subsequent image, acquired at 05:15, the plume detached from the volcano and traveled south 20 km. The velocities and temperatures of the plume produced during Phase One of the eruption were compared to the G2S wind field data for the region, suggesting that the plume reached altitudes between 6000 and 6600 m (Table 2).

Phase Two began at 5:45 when a new 4 km wide plume (Plume Two) was detected extending south 8 km from the summit. This plume continues to widen, until 07:15 when it reached its maximum width of 30 km. After 07:15 the leading edge of the plume shifted to the southwest, reaching a maximum distance of 50 km (Fig. 3c). At 07:45 the plume begins to separate with a portion still attached to the summit (source plume) and the leading edge forming a small, detached eruption cloud (Fig. 3d). The source plume was traveling south, while the eruption cloud was traveling to the southwest (Fig. 3d). The eruption cloud had completely separated from the source plume by 08:15. From 08:45 to 09:15 background meteorological clouds made distinguishing the eruption plume and clouds leading edge difficult; therefore estimates of how far the plume and cloud were transported could not be made. The second phase of the eruption was characterized by an increase in the plume's velocities and a decrease in plume top temperatures (Table 2). From 05:45 to 07:15 the height of Plume Two was estimated between 6000 and 8900 m (Table 2).

Phase Three began at 9:45 when a new plume (Plume Three) is observed at the summit, extending 8 km (Fig. 3e). The next three images (10:15–11:15) showed the plume still attached to the summit reaching a maximum width of 34 km and extending 52 km south of the summit (Fig. 3f). Velocities and temperatures of Plume Three when compared to the G2S wind fields suggest the plume rose to a higher altitude of 7200 to 10,900 m (Table 2).

Phase Four of the eruption started at 12:15 when there appears to be an increase in the eruption intensity. From 13:00 to 14:45 the image frame does not contain the full geographic area, but a portion of Plume Three,

which is within the summit region of the volcano, is observed (Fig. 3g–h). As time progresses the plume becomes wider at the summit region and darker, indicating cooler temperatures. After 14:45 it appears that the eruption has ended, for the plume is no longer visible in the GOES satellite imagery. For the fourth phase of the eruption the imagery was again cut off, not allowing the entire plume to be observed. Therefore, velocity and height estimates could not be calculated using the velocity determination or PTT method. Using data acquired from the Washington Volcanic Ash Advisory Center (VAAC) velocities determined during this time range suggest that the plume was transported at $\sim 5 \text{ ms}^{-1}$, and reached 14,300 m.

3.3. July 14th–15th 2006 eruption

The July 14th–15th 2006 eruption is broken down into three phases based on the plume dispersal patterns, velocities and heights (Table 3). Phase One began when a plume was first observed in GOES band 4 imagery on July 14th at 22:45 (Fig. 4a). The image revealed a small plume, 4 km wide, with a leading edge 8 km west of the volcano. The plume gradually increased both in length and width until 23:45 when an elongate umbrella cloud is apparent. On July 15th 2006, 0:15, the image is cut off but a large increase in the intensity of the eruption is apparent from the broadening in the plume's width near the vent and cooler plume temperatures as indicated by darker colors. At this point the plume appears bifurcated with movement to both the west and southwest (Fig. 4b). The western portion of the plume traveled 57 km from the vent and was 24 km wide. At 0:45 the movement was to the west–southwest and ongoing. Phase Two starts at 01:15 when the western component of the bifurcated plume is no longer prominent, showing minimal movement, and the principal component of movement was southwest (Fig. 4c). The plume continues to be transported to the southwest from 01:45 to 03:15. At 03:45 the larger eruption cloud that had previously obscured the volcano drifted to the southwest, revealing the vent (Fig. 4f) and indicates the beginning of Phase Three. At this time a smaller plume is observed attached at the vent and traveling to the southwest. A MODIS image was also collected at 03:50 showing a large eruption cloud extending $157 \times 117 \text{ km}$. It shows that a distinct portion of the plume is still attached to the vent (Fig. 5a). At

Table 4
August 16th–17th 2006 eruption plume temperatures, velocities and estimated plume top heights as well as additional comments about the plume's dispersal patterns.

Phase	Date/time (UTC)	Min temp (°C)	Min height (m)	Max height (m)	Velocity (m s ⁻¹)	Min height (m)	Max height (m)	Comments	
1	8/16/2006 20:15	-7	6000	6250	*	6250	7000	Plume first observed in TIR imagery. Thin plume traveling to the west of the vent	
	8/16/2006 20:45	-6	6000	6250	*	6250	7000	Thin plume traveling to the west of the vent	
	8/16/2006 21:15	-6	6000	6250	*	6250	7000		
	8/16/2006 21:45	-4	5500	5750	*	6250	7000		
	8/16/2006 22:15	-4	5500	5750	*	6250	7000		
	8/16/2006 22:45	-7	6000	6250	*	6250	7000		
	8/17/2006 00:45	-8	6250	6500	*	6250	7000		
	8/17/2006 1:15	-8	6250	6500	2.0	6250	7000	Plume increases in width and length	
	8/17/2006 1:45	-12	7000	7250	2.3	6250	7000		
	8/18/2006 2:15	-15	7000	7250	1.5	6250	7000		
2	8/17/2006 2:45	-20	8500	8750	2.0	6250	7000	Plume continues to grow in length and width	
	8/17/2006 3:15	-25	9000	9250	5.0	11,500	11,750		
	8/17/2006 3:45	-28	9500	9750	5.0	11,500	11,750		
	8/17/2006 4:15	-59	13,000	13,250	10.0	11,500	11,750	New pulse in the eruption. Plume increases in width near summit region	
	8/17/2006 4:45						Data gap		
	8/17/2006 5:15						Data gap		
	8/17/2006 5:45						Data gap		
3	8/17/2006 6:15	-73	15,500	15,750	*			Large circular plume observed (156 × 134 km) velocity measurements could not be made due to data gap.	
	8/17/2006 6:45	-78	17,250	17,500	*			Plume is spreading concentrically, no principle direction of motion detected, therefore no velocity measurement were calculated. Velocity and temperatures listed in this section below are for the portion of the plume being transported to the east.	
4	8/17/2006 7:15	-78	16,500	16,750	12.4	22,250	24,000	Plume begins to be dispersed to the east	
	8/17/2006 7:45	-76	15,750	18,250	12.4	22,250	24,000	Plume begins to be transported to the east.	
	8/17/2006 8:15	-74	14,500	14,750	12.4	22,250	24,000	Movement to the west is also observed (see below)	
	8/17/2006 8:45	-69	14,000	14,250	12.4	22,250	24,000	After 8:45 the leading edge of the eastern component is difficult to discern, therefore temperature and velocity measurements are not accurate and not reported. Velocity and temperatures listed are for the portion of the plume moving to the west.	
		8/17/2006 7:45	-65	14,000	14,250	2.1	7250	10,500	
		8/17/2006 8:15	-62	13,500	13,750	2.1	7250	10,500	
		8/17/2006 8:45	-54	12,500	12,750	2.1	7250	10,500	
		8/17/2006 9:15	-51	12,000	12,250	2.1	7250	10,500	
		8/17/2006 9:45	-43	11,250	11,500	2.1	7250	10,500	
		8/17/2006 10:15	-31	9750	10,000	2.1	7250	10,500	
	8/17/2006 10:45	-25	9000	9250	2.1	7250	10,500		
	8/17/2006 11:15	-20	8500	8750	2.1	7250	10,500		

Asterisks indicate values could not be determined.

04:15 the smaller plume is still attached, but is weaker in intensity as indicated by the lighter colors and hence the warmer temperatures (Fig. 4g). From 04:45 to 06:45 the attached plume continues to travel to the west (Fig. 4h–i). A second MODIS image was collected at 06:45 and shows the large eruption cloud has dispersed and that there is a smaller eruption plume traveling 40 km to the west–southwest (Fig. 5b). The eruption appears to have ceased sometime after 06:45 when the smaller plume is no longer observed in the imagery.

Comparing the velocities and temperatures of the eruption plume (Table 3) with the G2S wind field data suggests that the transport of the plume could be divided into three periods. Initially, the plume was at low altitudes (6000–6250 m), followed by a drastic increase in plume heights (14,250–14,500 m) to the maximum height the plume reached in the eruption. Once the initial large eruption cloud dispersed, the satellite images revealed that there was still a small plume attached to the vent being transported to 6750–8000 m. Measurements taken from the MODIS images collected during the eruption suggest the plume was traveling at slightly higher altitudes of 9000–9250 m and 7750–8000 m at 03:50 and 06:45, respectively.

3.4. August 16–17th 2006 eruption

The eruption and dispersal of the volcanic plume emitted during the 16–17 August eruption of Tungurahua can be broken into 5 different phases based upon the style and direction of transport of the

plume as well as the determined plume heights. Phases of the eruption, temperatures, velocities and plume heights are given in Table 4.

The first phase occurred between 20:15 and 02:15 UTC and was characterized by the emission of a low-altitude, short-lived, low intensity plume. The second began at 02:45 on August 17th 2006 and ended at 04:45, with an increase in intensity of the plume from the first phase. This was followed by a highly explosive third phase between 06:15 and 06:45. The fourth phase lasted from 07:45 to 11:45 and is characterized by the transport and dispersal of the eruption cloud. The final fifth phase began at 11:45, and lasted until the plume fully dissipated, and is only characterized by transport of the plume. Since ash dispersal is not the primary objective of the paper the final phase is not discussed in length.

Phase One of the eruption began at 20:15 on 16 August 2006 when the eruption plume was first observed in GOES band 4 satellite imagery. The image showed a 4 km wide plume extending approximately 70 km west of Tungurahua (Fig. 6a). The plume length remained fairly constant for approximately 4 h (Fig. 6 a–d). During the same period a MODIS image was acquired (19:05) and captured a small plume reaching 16 km to the southwest (Fig. 5c).

On August 17th 2006 02:45 the initiation of Phase Two was indicated by an increase in plume width (16–20 km) and plume length (90 km) (Fig. 6c). The direction of movement shifted from 270° N to 285° N. This activity remained constant until 4:15 when the

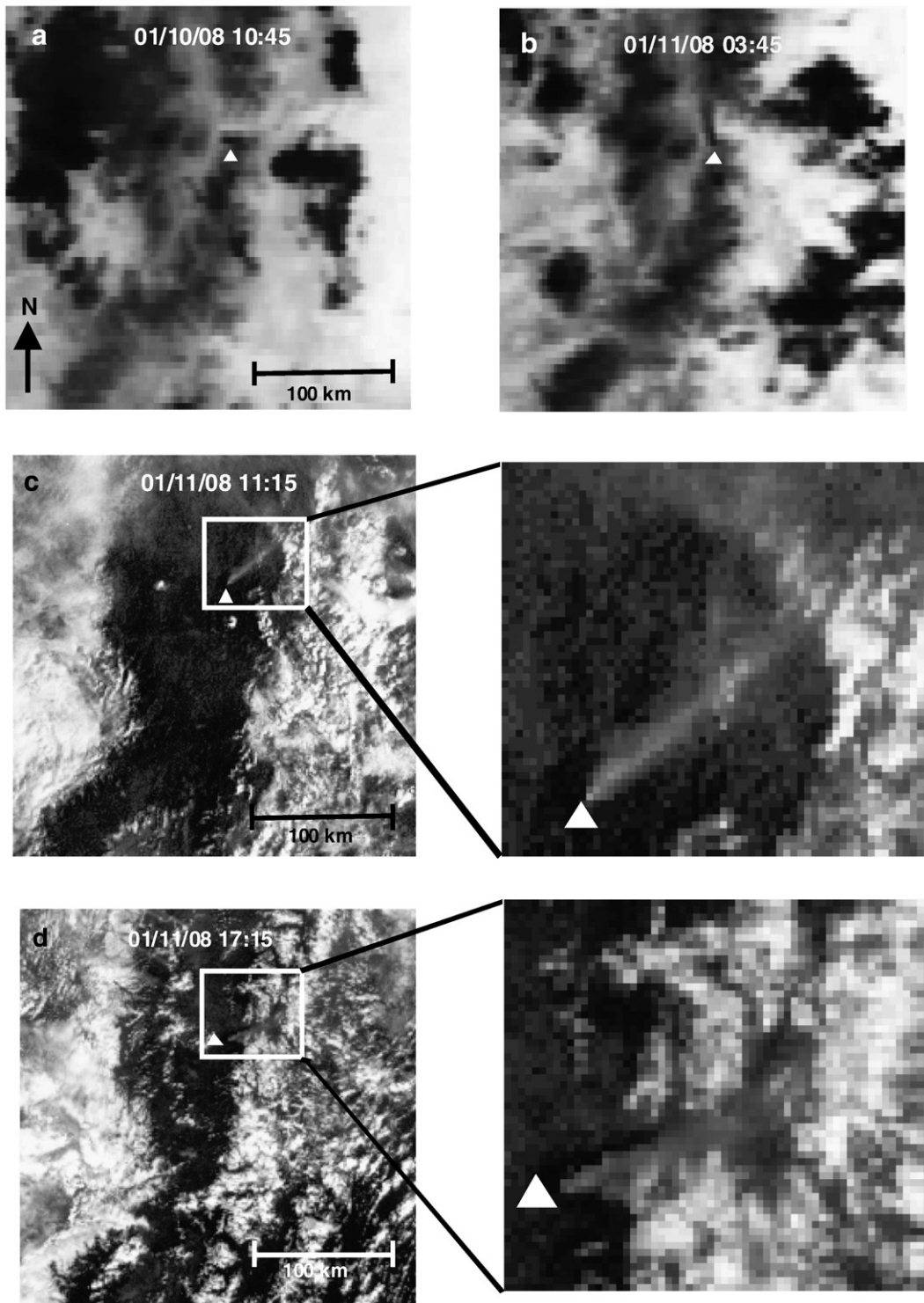


Fig. 2. GOES imagery of the January 2008 eruption sequence. a – GOES TIR image acquired on 1/10/08 10:45 displaying a small eruption plume traveling 8 km east of the summit. b – GOES TIR image acquired 1/11/08 3:45 showing a small eruption plume traveling 20 km north of the summit. c – GOES VIS images acquired on 1/11/08 11:15 displaying a small eruption plume traveling 32 km northeast of the summit and d – GOES image acquired later in the day at 17:15 indicating a small plume was traveling 33 km east/northeast of the summit.

image showed a new, thicker (24 km), and darker portion of the plume near the vent (Fig. 6d).

A data gap occurred between 04:45 and 05:45 and no images were acquired. At 6:15 a new image was acquired and a large circular umbrella cloud was apparent above Tungurahua, which indicated that the onset of Phase Three occurred sometime between 04:45 and 06:15. The plume measured 156×134 km in length and width, respectively (Fig. 6e). In the following image (06:45) the plume did

not have a principal direction of movement; instead it spread radially from the source of injection. The uninterrupted, continuous infrasonic data provides insight into the chronological progression of Phase Three, as will be discussed in a later section.

The fourth phase began at 07:15 (Fig. 6f) when the image shows the plume had a principal direction of dispersal (90° N), indicating wind had taken over the transport of the plume. At this time the clouds leading edge was transported 26 km from its location in the

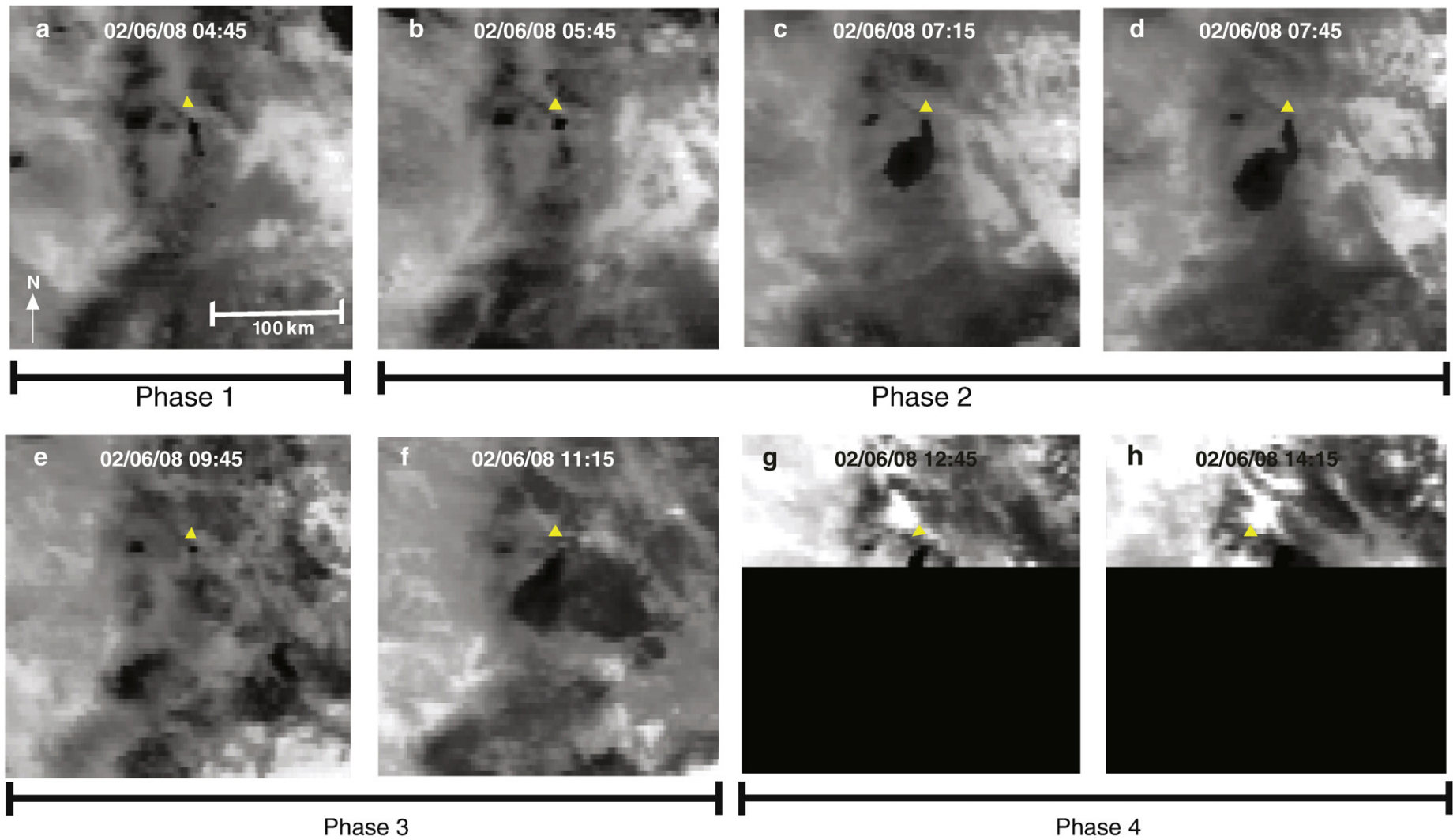


Fig. 3. GOES TIR imagery acquired during the February 2008 eruption. In panels a–h small eruption plumes are observed in GOES TIR imagery throughout the eruption sequence traveling south/southwest of the volcano reaching a maximum distance of 80 km from the summit. Between 7:15 and 7:45 shearing of the plume occurs, causing the plume to separate into two sections, an eruption cloud and a plume that is still attached to the summit (panels c and d).

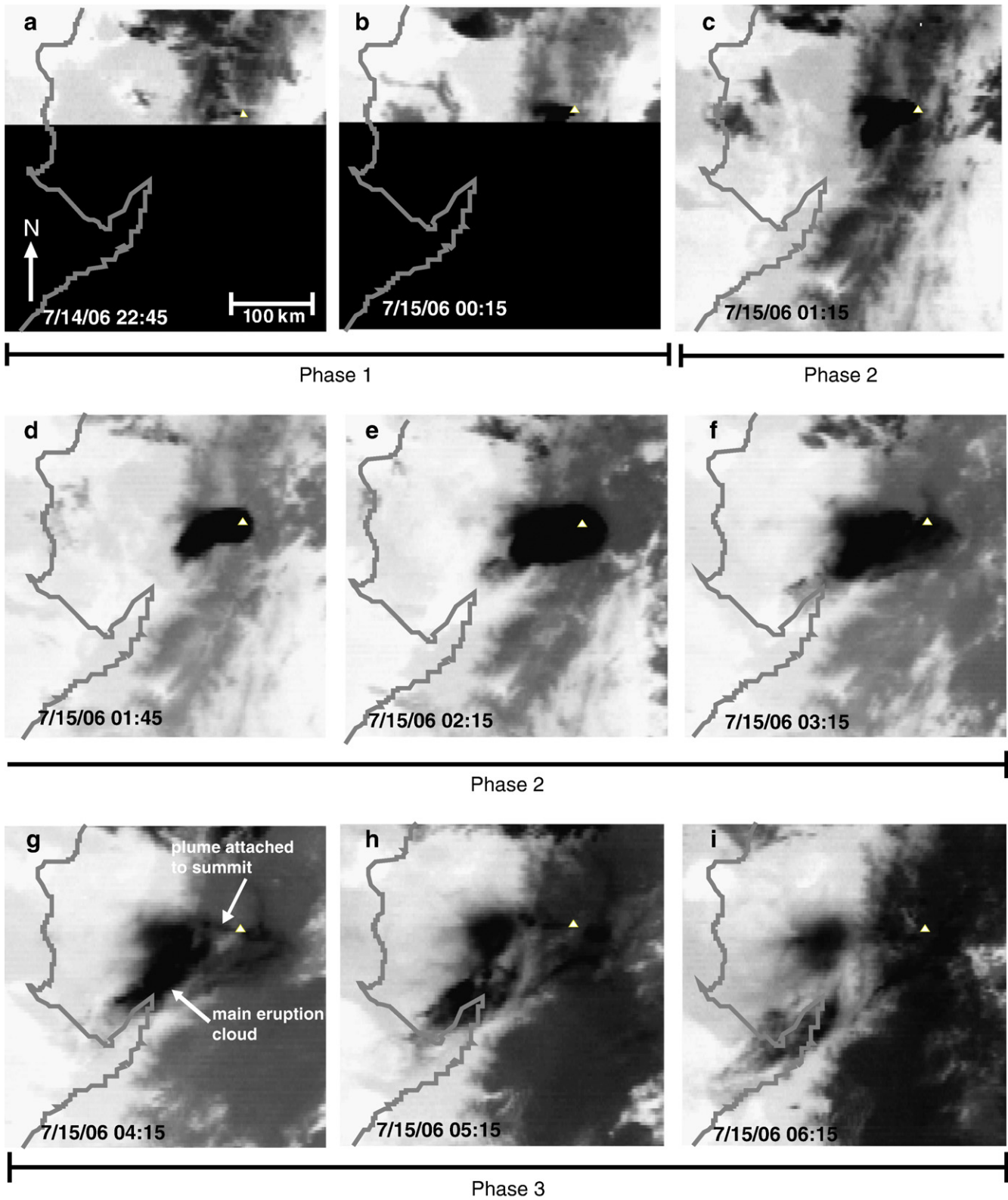


Fig. 4. GOES imagery collected during the July 2006 eruption. GOES TIR imagery showing the eruption sequence for the July 14th–15th 2006 eruption. The eruption started as a small eruption plume traveling the west (panel a) that consistently grew in length and width (panels b–f). The eruption cloud was transported to the west/southwest and at 4:15 the summit is visible with a smaller plume still attached to the summit, indicating that the eruption was still occurring (panel g). No activity was observed at the summit in satellite imagery after 6:15 (panel i).

previous image, traveling a total of 98 km from the vent (to the east). At 07:45 a secondary direction of motion is observed (270° N); the eruption cloud was traveling to the east and the west (Fig. 6g) at different altitudes. Transport of the cloud continued to the west and

east until 11:15 when the leading edge of the eastern component was no longer observed in the satellite imagery.

Phase Five began at 11:45 when the eruption cloud was just being dispersed to the west. This phase lasted until the end of the day

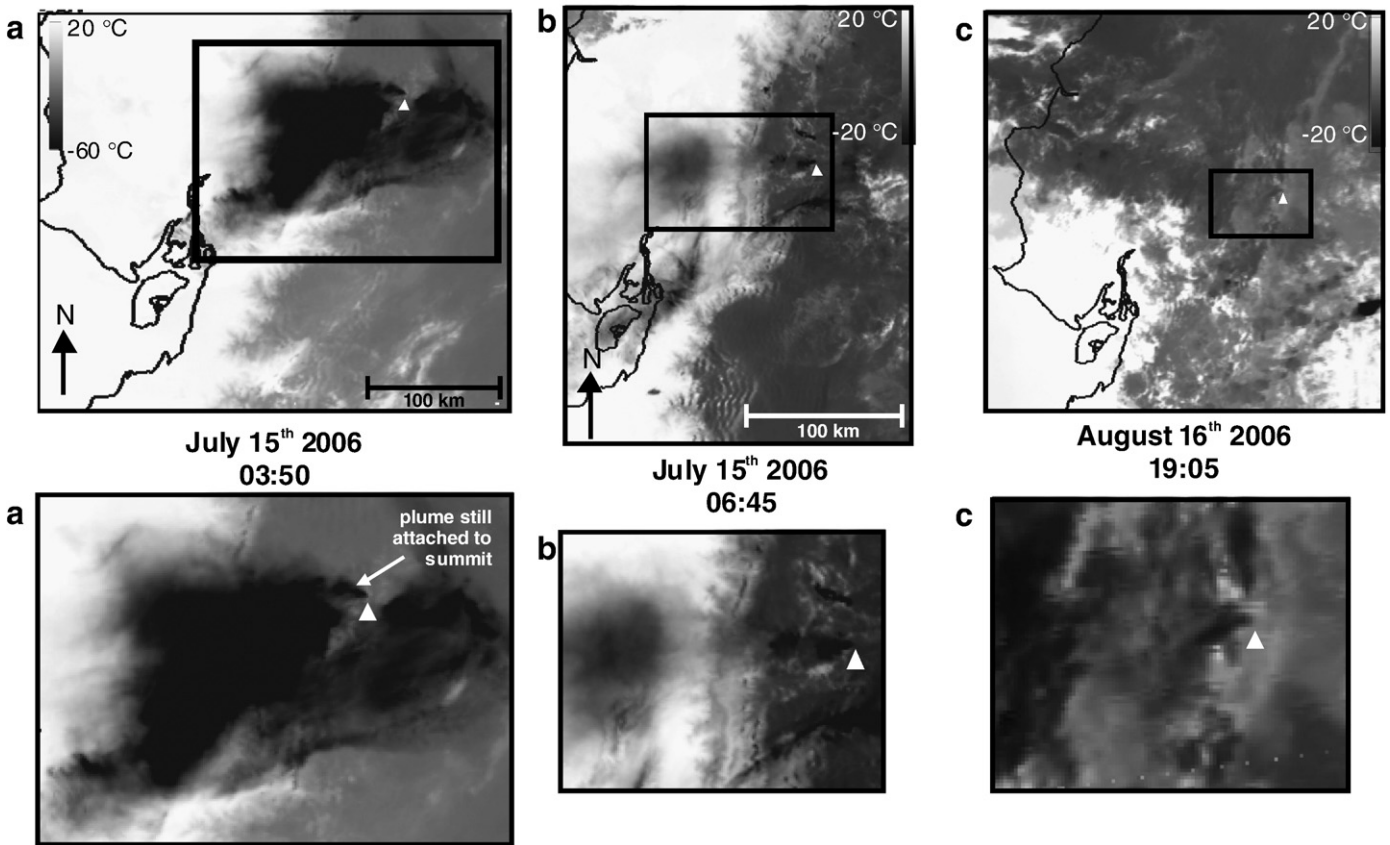


Fig. 5. MODIS imagery acquired during the July and August 2006 eruptions. a – MODIS TIR (band 32) image collected on 7/15/06 at 3:50 showing the eruption cloud traveling to the west/southwest with the plume still attached to the summit, indicating the volcano was still erupting. b – MODIS image collected on the same day at 6:45 showing the eruption cloud has been transported to the west/southwest and has dissipated. No activity is apparent at the summit region, indicating that the eruption has ended. c – MODIS image collected on 8/16/06 at 19:05 showing a small eruption plume traveling west of the volcano's summit region.

(14:45) when the eruption cloud was no longer visible in the satellite images. The vent of Tungurahua was observed once the plume was transported and dispersed at 13:15, and no further explosive activity was detected.

The satellite-derived ash plume heights inferred from the velocity and temperatures measurements can also be broken down into five phases (Table 4). During Phase One of the eruption the plume was initially being transported at low altitudes with maximum heights ranging between 6250 and 7250 m. Measurements gathered from MODIS imagery constrain those heights between 7000 and 7250 m. Phase Two was characterized by a gradual increase in plume heights reaching a maximum altitude of 13,250–15,250 m at 04:15. During Phases Three and Four the large umbrella cloud was being dispersed at two different elevations: the higher between 17,500 and 24,000 m and a lower between 7250 and 10,500 m. During Phase Five the plume dispersal continued as in the previous phase.

4. Interpretation of eruptive events and eruption classification

This section discusses the different eruption mechanics responsible for changes in plume heights and dispersal patterns inferred from combining satellite data, FLIR and infrasound signals (Fee et al., in press) recorded during the different eruptions at Tungurahua during this study period. The acoustic power levels quoted here are averaged over 15 minute time intervals, are given in watts (W) or megawatts

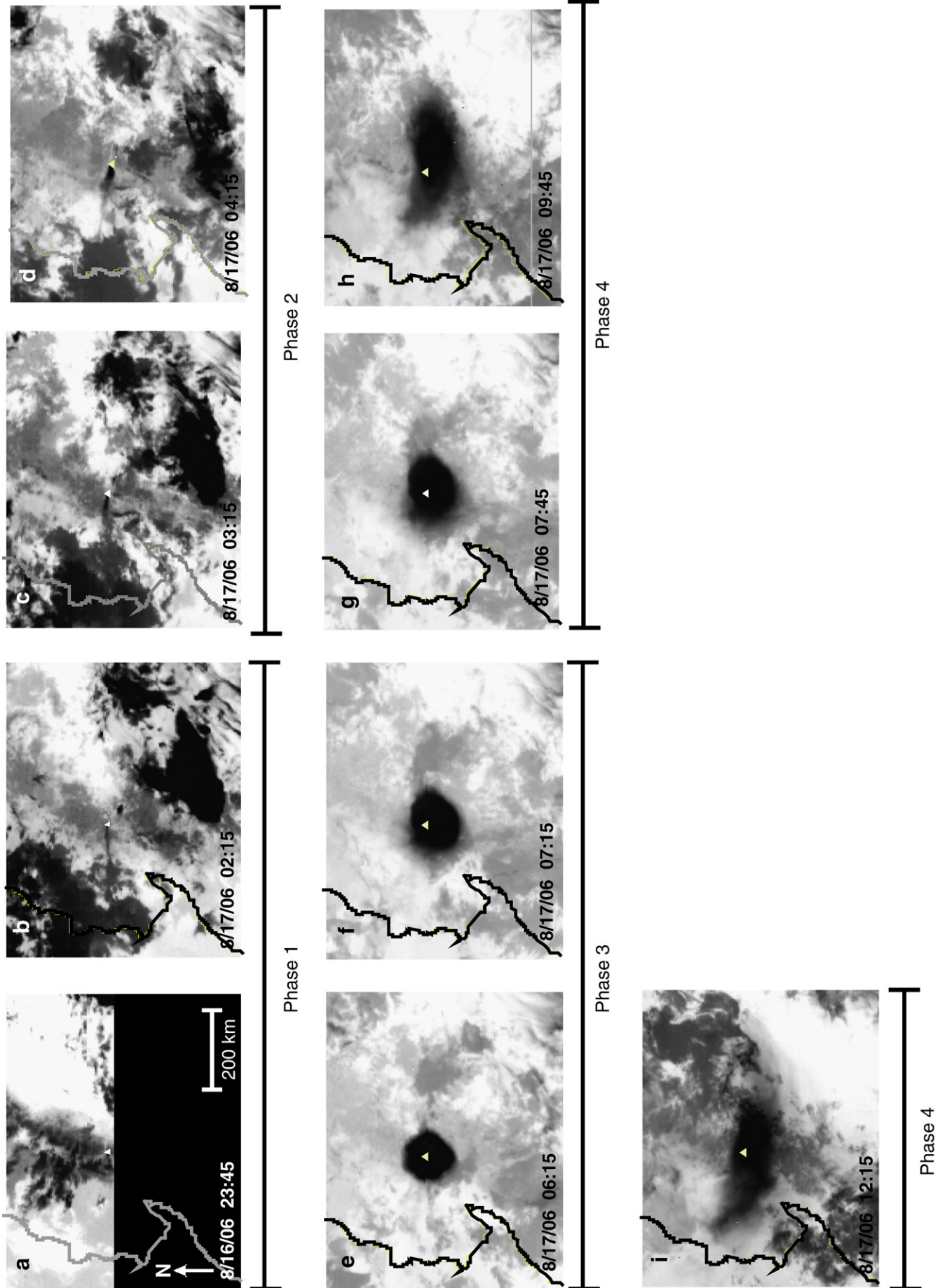
(MW, 10^6 W). Unless otherwise stated, all energy values are estimated in the frequency band between 0.1 and 4 Hz, which may underestimate total power if there is a substantial contribution outside this passband.

To report the possible range of heights reached by the eruption clouds during the various eruptions we have combined the heights obtained using both the PTT and velocity determination method. The minimum and maximum heights reported are therefore the minimum and maximum obtained from both methods giving the widest range of heights. Height discrepancies will be discussed on a case by case basis.

4.1. January 10–11th 2008

The maximum and minimum plume heights of the January 2008 eruptions are shown in Fig. 7a. Both eruptions are characterized by continuous low-level plumes of nearly constant height. Variations in plume heights are observed on January 11th 2008 at 04:45 and 06:45 which are consistent with increases in the acoustic power which increments from 4.5×10^4 to 1.7×10^5 W (Fig. 7a). The relatively low power levels (in comparison to over 50 MW of radiated sound power in August 2006) are in agreement with the low plume heights as well as the fact that the plumes on January 11th could not be detected in the TIR bands. This means that the plume was not large enough or had a lower ash content that inhibited detection in the lower-spatial resolution thermal band.

Fig. 6. GOES imagery collected during the August 15th–16th 2006 eruption. The eruption started at 23:45 with a small plume traveling to the west (a). As the eruption continued the plume gradually grew in length and width (b–d) but then a data gap occurred between 04:45 and 05:45. The next image acquired at 06:15 shows a large umbrella cloud above the volcano (e). Initially the plume grew radially from the source (f), but was later transported to the west (g) and then to the east (h). The bidirectional plume is caused by an atmospheric wind shear.



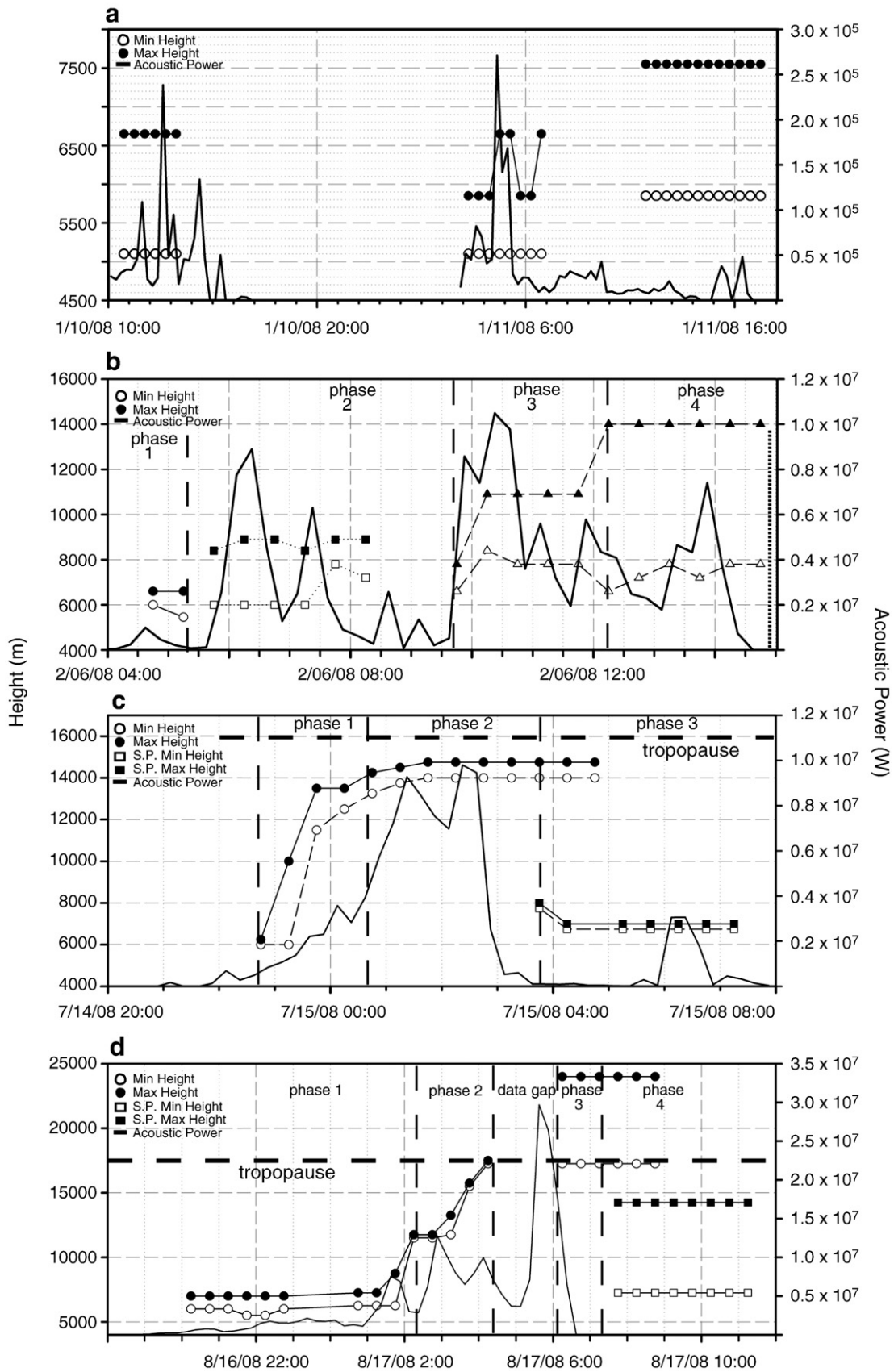


Fig. 7. Plume heights and acoustic power produced during Tungurahua eruptions. The range of eruption cloud heights and corresponding acoustic power from the Tungurahua eruptions in January 2008 (a), February 2008 (b), July 2006 (c) and August 2006 (d). Range of eruption cloud heights were determined by combining two methods (velocity and PTT) while acoustic power was calculated using frequencies above 0.1 Hz. It should be noted that, including a wider range of frequencies would lead to higher power levels, in particular for the 17 August eruption (d) where the total acoustic power would reach above 50 MW. Timing of eruption clouds observed in imagery and acoustic power correlates well for all eruptions under investigation. Also, a good correlation is observed for maximum plume height and acoustic power for plinian (d) and sub-plinian (c) eruptions, with correlation for weaker eruptions decreased (a and b).

4.2. February 6th 2008

The February eruption was characterized by several explosions, resulting in short-lived, low-altitude plumes followed by a larger sustained eruption. The eruptions were well documented in satellite and infrasound data, but unfortunately no FLIR imagery was available for the eruption sequence. Although an eruption plume was first detected in GOES imagery at 04:45, the eruption onset (as inferred from the infrasound data) occurred ~20 min earlier. Jetting was first recorded in the infrasound signal at 04:25, indicating an increase in volcanic activity. The plume had a height of 6000–6600 m. In the subsequent image (05:15) the plume height is lower than in the previous image (5450–6600 m) and has detached from the summit. This also correlates well with the estimated infrasound power, which decreases between 05:00 and 05:40 from 2.04×10^5 to 7.68×10^4 W (Fig. 7). This decrease in the infrasonic jet noise energy is consistent with the plume detachment from the summit. Since jetting is still occurring during this time the eruption has not ended but only diminished, with possible lower ash concentrations that may not be distinguishable in the satellite imagery.

A new plume was observed in the GOES data between 05:45 and 08:15, reaching a maximum height of 6000–8900 m at 06:15, which remained at this height until 08:15 (Fig. 7b). Again this correlates with the infrasound power (8.9×10^6 W) specifically increased jetting and the signal becoming more broadband between 05:40 and 06:55 (Fee et al., *in press*), indicating an increase in intensity. Between 07:00 and 08:30 another jetting episode occurred with power levels decreasing slightly to 6×10^6 W, but the signal had a different infrasound signature than the previous episode with more variability in frequencies greater than 2 Hz (Fee et al., *in press*). The change in the acoustic signal is reflected by changes in the dispersal pattern of the plume. Although the plume heights do not change, the plume begins to separate (Fig. 3c and d). Changes in the plume's dispersion could be the result of the plume reaching slightly higher or lower altitudes that might not be detected in the remote sensing techniques, or the atmospheric stratifications might be smaller than the vertical grid spacing represented by the atmospheric profiles. Between 08:45 and 09:15 the plume is difficult to distinguish in the satellite imagery and it appears at first that the plume might be obscured by meteorological clouds. However the infrasound signal decreases during this time, from 6.3×10^6 to 7.9×10^4 W, indicating that although there is continued activity at the vent, the plume may not be as ash-laden or large enough to be detected in the satellite data.

Following this period of decreased activity, the most energetic portion of the eruption occurs, reaching the highest altitudes in the eruption sequence. Between 09:45 and 11:45 a new plume is observed in the GOES imagery that grows in size (30 × 45 km) and by 10:15 it reached a maximum altitude of 6600–10,900 m. The entire eruption plume cannot be seen in the satellite imagery so the height estimates are based on the coldest temperatures that are observed in the imagery. Reports from the Washington VAAC indicate that the plume reached a higher altitude of 14,000 m which we find reasonable given the intensity of the infrasound signals. During this time period the most energetic jetting of this eruption sequence reached acoustic power levels of 1×10^7 W (Fig. 7). Again the most energetic acoustic signals occur just before the highest plume heights were reported by the VAAC.

4.3. July 14–15th 2006

The July 2006 eruption was characterized by a steady increase in plume heights and acoustic power, followed by a sharp decrease. A plume was first detected in satellite imagery at 22:45 having attained a height ranging between 6000 and 6250 m. Since no imagery was collected during the start of the eruption the infrasound signal constrained the onset of the eruption. The start of the eruption is

identified by the onset of jetting and an explosion signal at 22:34. Between 23:00 and 0:45 the plume steadily rose in altitude reaching its maximum height of 13,750–14,500 m at 01:15 (Fig. 7c). From 22:34 to 0:00 the acoustic power levels also steadily rose from 1 to 3.5 MW (Fig. 7c). This steady rise was followed by a rapid increase between 0:00 and 01:00 with power increasing from 3.0 to 4.5 MW. Jetting occurs at lower frequencies (<1–2 Hz) between 01:00 and 02:00 (Garces et al., 2008; Fee et al., *in press*) and the sound power rises reaching a maximum of 9.8 MW at 01:25. The power levels then drop off rapidly at 03:00 to 0.53 MW, indicating the most intense portion of the eruption had ended. The plume heights remained constant between 13,750 and 14,500 until 03:15.

Although the plume heights and infrasound correlate during for the first portion of the eruption (22:45–01:15) during the latter portion there is less correlation. The reason that the satellite-derived plume heights may not be expected to correlate with the infrasound signals during these times is because the two sensors are measuring different processes. The satellite sensor is detecting the maximum height reached by the eruption cloud emitted during the most energetic event. That eruption cloud obscured new plume emissions and activity occurring beneath it. However, the infrasound sensors are detecting the activity that is occurring near the vent. Thus it is possible that during this time period the eruption intensity has decreased, but the satellite sensor cannot detect this because the vent is being obscured by the eruption cloud that was injected into the atmosphere during the earlier (most energetic) event.

For this time period FLIR imagery was also sporadically collected. An image collected at 01:22 (Fig. 8a) indicates that the eruption column had a sustained convective region, with an estimated height of ~1.8 km. In the next FLIR image collected at 02:50 the column has collapsed and is feeding pyroclastic density currents (PDCs) (Fig. 8b). This correlates well with the infrasound record that shows a decrease in acoustic power (Fee et al., *in press*). There are several factors that can cause a sustained column to collapse. The most common are lower exit velocities, increase in the amount of lithics (decrease in gas content), or the widening of a vent (Sparks et al., 1978; Sparks et al., 1997; Branney and Kokelaar, 2003). Although it is difficult to distinguish the exact cause of collapse during this eruption and multiple factors may be involved vent widening was documented at the end of the eruption.

By 03:15 the largest eruption cloud from the initial event was transported to the southwest, allowing the vent to be observed in the satellite imagery. A plume is still attached to the vent, but the heights decreased to 7500–8000 m (Fig. 7c). The plume height decreases at 05:45 to 6750–7000 m and remains at this height until the plume is no longer observed in satellite imagery (6:45) (Fig. 7c). The infrasound data during this time also shows a decrease in activity with the acoustic power dropping suddenly at 03:00 from 9.4 to 0.53 MW (Fig. 7c). Steady tremor (1.4 Hz) resumed after 03:00. Again, this decrease in acoustic power indicates changes in the eruption dynamics and it is now likely that the plume observed is caused by PDCs, similar to those observed earlier in the hand-held thermal imagery. The most energetic portion of the eruption therefore ended at 03:00. The FLIR imagery collected prior to this time period indicates that there are sustained pyroclastic density currents, but after 03:06 there are sporadic PDCs, most likely resulting from small dome collapses instead of a sustained collapsed column (Fig. 7c). This shows that the activity at the summit has decreased, compared to earlier phases in the eruption, inhibiting the plume reaching altitudes reached during the most energetic phase of the eruption.

4.4. August 16–17th 2006

The largest eruption observed during this study period was the August 16th–17th 2006 sequence. It was characterized by an initial gradual increase in plume heights followed by a dramatic increase in plume heights and acoustic power, followed by a sudden end in eruptive

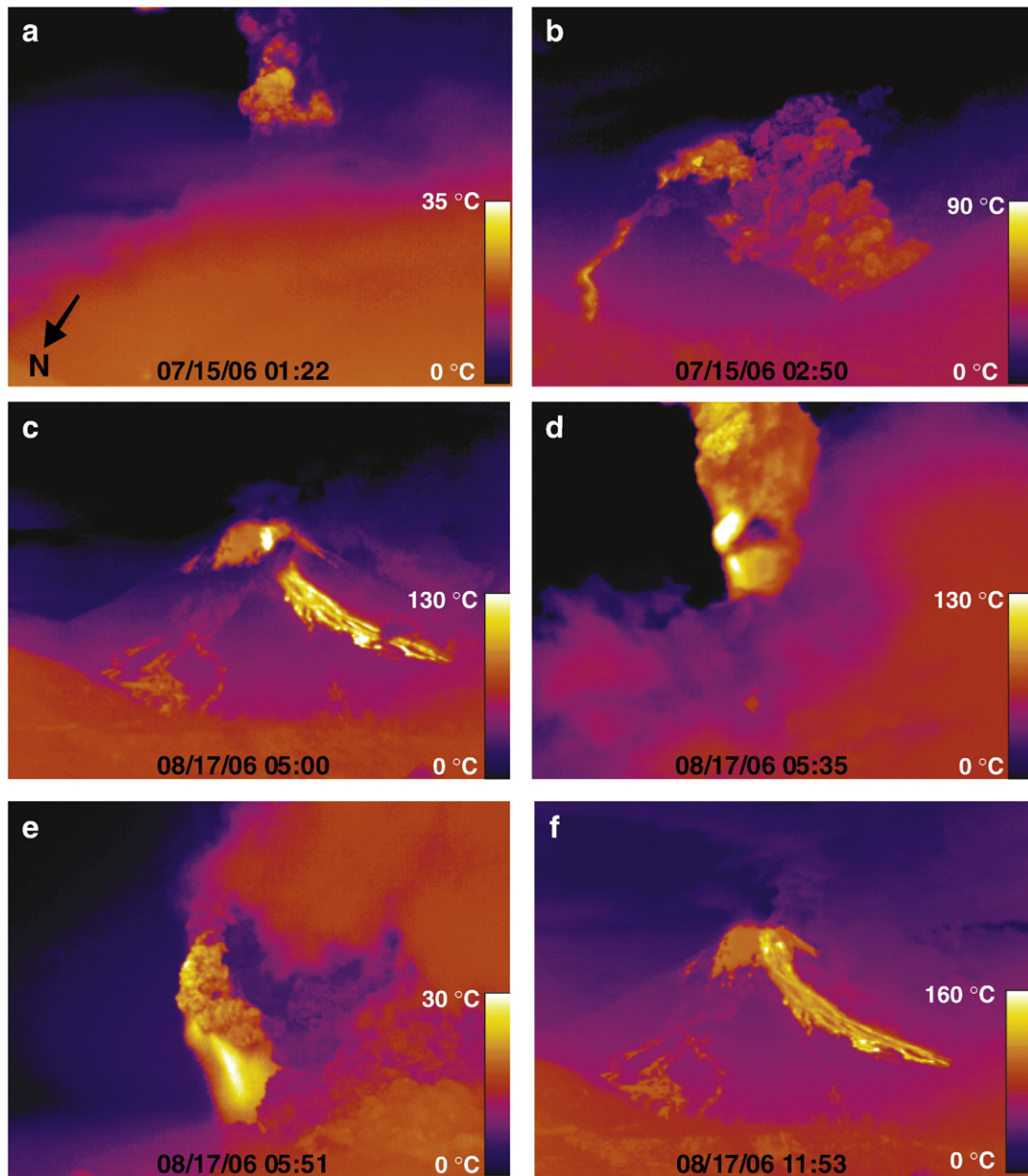


Fig. 8. FLIR imagery collected during the July and August 2006 eruptions. FLIR imagery showing changes of vent processes during the different eruptions. a–b – Images collected during the July 2006 eruption indicating that initially the plume was fed by a sustained column (a) which later collapsed and resulted in a series of PDCs (b). c–f – Images collected during the August 2006 eruption show that initially the eruption was less energetic, fed by a PDCs (c) followed an energetic portion of the eruption with a large sustained column (d and e). The final image collected after the end of the eruption shows warm PDC deposits on flanks, with no activity at the summit region (f).

activity (Fig. 7d). From the satellite imagery the eruption was first detected by GOES at 20:15 as a persistent emission of a plume to a steady height of 6000–7250 m until 02:15 (Fig. 7d). The infrasound data suggests that the eruption began earlier at 19:30 as indicated by the emergent onset of jetting. The infrasound data also indicates a change in eruption dynamics with increased jetting power levels rising from 8.7×10^4 to 6.3×10^5 W from onset (20:20) until 21:30. A possible reason why the changes in infrasound intensity are not detected in satellite imagery is the infrasound sensors can detect small changes in the source intensity that may not have produced significantly different plume heights. The plume heights then suddenly increased from 01:00 to 03:45 (Fig. 7d) indicating an increase in eruption intensity. This corresponded with an increase in the acoustic power during the same time period, peaking at 8 MW (Fig. 7d). Between 03:45 and 04:15, the plume heights rose suddenly again with heights of 11,500–13,250 m (Fig. 7d). During this time the power levels increased from 8.0 to 10.0 MW (Fee et al., in press). Although it is difficult to determine what could

cause an increase in plume height that would not be detected in the infrasound, some speculations can be made. One possible explanation could be that the plume was being fed by the PDC's and not a sustained column. It is known from the hand-held thermal imagery and visual reports that PDC's were forming around this time due to column collapse (Barba et al., 2006). If these smaller increases in mass flux (that are observed in the infrasound data) are supplying enough hot material to the currents this would allow the elutriation of the fines (fine grained ash particles) within the PDC's that would form a rising convective plume. Therefore, the plume could rise to higher heights without the associated infrasound signal from the vent. A column versus PDC fed plume cannot be distinguished in the satellite imagery due to the low spatial resolution of the sensors. These types of PDC fed plumes have been observed at several volcanoes, but one of the most notable is the 1989 eruption of Mt. Redoubt Alaska, which resulted in plumes reaching 12,000 to 13,500 m (Miller and Chouet, 1994; Schneider and Rose, 1994).

A GOES data gap occurred between 04:15 and 05:45 (August 17th), but during this time a further increase in eruption intensity occurred as shown by the infrasound and FLIR imagery. At 04:36 an energetic explosion is followed by intense and broadband jetting (Matoza et al., 2009; Fee et al., in press), with power levels reaching 0.7–1.0 MW (Fig. 7d). The paroxysmal and plinian phase of the eruption occurred between 05:30 and 06:20. At 05:30 the power levels increased to ~30 MW and jetting shifts to frequencies lower than 0.1 Hz (Garces et al., 2008; Matoza et al., 2009; Fee et al., in press) indicating a dramatic increase in the jetting. It should be noted that the acoustic power is an underestimate since it was calculated only using frequencies above 0.1 Hz (the lower frequency response of the sensor). The addition of lower frequencies increases the total acoustic power to >50 MW. This transition was also reflected in a change in activity recorded in the FLIR imagery (Fig. 8). At 04:53 the thermal imagery shows a smaller and less developed column, but after a data gap the imagery shows a sustained column with a large gas thrust region at 05:35 (Fig. 8d). In addition visual reports indicate that an incandescent jet reached heights up to 6000 m (Barba et al., 2006). The satellite imagery at 06:15 reveals a large circular eruption head, indicating that a large umbrella cloud (156 × 134 km) had developed (Fig. 6e) with plume heights reaching 16,000–20,700 m (obtained from PTT measurements). For the next hour the plume was controlled by gravitational spreading as evident from the plume spreading radially from the injection source, even against the prevailing wind fields (Fig. 6f). This indicates either the plume was not advected into the wind fields, and therefore the wind fields did not have control of the dispersion and transport of the plume, or that the hot jet flow substantially altered the atmospheric circulation in the region around the volcano. At 6:20 the acoustic energy decreased (Fig. 7d) drastically to 6.6 MW and 15 min later dropping to 1.8×10^4 W indicating that the most energetic portion of the eruption had ended.

Although there was no longer jetting activity occurring at the vent, the eruption cloud was still present. It is not until 07:15 that we could determine that a portion of the plume had been injected into the stratosphere and surpassed it by several kilometers. A principle movement of direction to the east was recorded at this time indicating that the eruption cloud had been advected in the wind fields and was no longer gravitationally driven. During the summer season at this latitude the only eastwardly moving winds (above the volcano's summit) are located above the tropopause. Thus, from the wind field data we can say, with certainty, that the plume reached 22,250 m, penetrating the stratosphere. We therefore conclude that the plume had reached heights to at least 22,250 m, and possibly higher, when the plume was first observed in the satellite imagery (06:15) (Fig. 6e). At 7:45 the satellite imagery indicates that the eruption cloud is also being transported to the west at a lower elevation. Therefore we know that the eruption was large and powerful enough to have been injected into the stratosphere, but that a portion of the plume was also being transported to the west at a lower elevation. Again, with the datasets available it is difficult to distinguish what caused the plumes to travel at two different elevations, but two different scenarios could cause such a phenomenon. The first is caused by the formation of lower secondary intrusion that is transported at a lower elevation due to an atmospheric shear zone with two fronts moving at opposite directions (Holasek et al., 1996b). Such shear zones are common in our heterogeneous atmosphere. After the emplacement of a large umbrella cloud it is possible for the cloud to decouple into two layers, a lower dense ash-ridden layer and an upper layer with more buoyant gas and fines rich layer. In our case the gas and fines rich layer was transported to the east, while the ash-ridden layer is being transported to the west. Such a separation would be consistent with satellite observations in which the higher layer became more diffuse and thus was not able to be detected by the satellite sensor (as would be expected if there was only gas and finer ash particles) (Fig. 6h). The lower, ash rich, layers dispersal could be tracked for several hours longer because it was still within the satellite's

detection threshold. The next scenario is that the two clouds are being fed by two different sources; the higher portion of the plume is being fed by the plinian eruption column while the lower cloud is being supplied by a PDC. During the paroxysmal phase of the eruption PDC's were documented, therefore these currents could have been supplying a large PDC that was elutriating the fines within the current, leading to a PDC feeding a smaller convective column, that would be transported to the west. This has also been observed at other large stratospheric eruptions such as Mount St. Helens (e.g. Sparks et al., 1986; Holasek and Self, 1995) and Mount Pinatubo (e.g. Holasek et al., 1996b; Tupper et al., 2005). Both scenarios are possible, since a shear zone was observed in the wind field data and pyroclastic density currents were documented, and it is difficult to distinguish between the two from the data available.

The eastern and western movement of the plume continues until the eruption clouds dissipate to the point at which they could no longer be observed in the satellite imagery. This had occurred by 13:15, when the eruption cloud was diffuse enough to observe the vent. This image agrees with the infrasound observations that suggested the eruption ended 7 h earlier. The FLIR imagery collected at 11:53 also indicated no new explosive activity, but instead cooling pyroclastic and lava flows (Fig. 8f).

5. Classification of eruption intensity

Classification of eruptions is a difficult task as many of the different types of eruptions share overlapping characteristics. Eruption

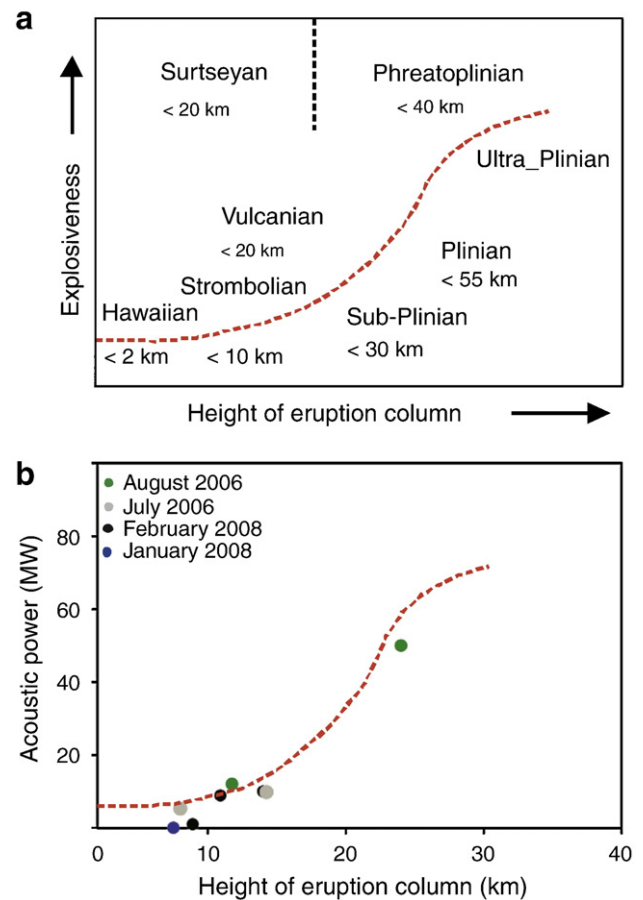


Fig. 9. Eruption classification based on field based measurements versus those made by acoustic power and eruption plume height. a – Adapted from Walker (1973) and Cas and Wright (1988) shows a classification scheme based on explosiveness and height of eruption column. b – Classification for Tungurahua's eruptions during 2006–2008 based on peak acoustic power and height of the eruption column. Note that there is a similar trend observed when comparing explosiveness (a) and peak acoustic power (b). Plinian and sub-plinian eruptions are easily classified, but distinguishing between vulcanian and strombolian explosions is more difficult and more information is necessary.

Table 5
Parameters used in eruption classifications.

Date	Maximum height (m)	Plume/eruption cloud ratio	Estimated jetting duration	Maximum acoustic power (MW)	Intensity classification
1/10/08–1/11/08	7500	0.06–0.15	Transients	0.04	Strombolian to weak vulcanian
2/6/08					
Phases 1–2	6000	0.5	Transients	1.0	Vulcanian
Phase 3	10,900	0.6	2.5 h (not sustained)	8.9	Vulcanian
Phase 4	14,000	n/a	2.5 h (seven pulses)	10	Strong vulcanian
7/14/06–7/15/06					
Phases 1–2	14,250	0.7	5 h	9.8	Sub-plinian
Phase 3	8000	~0.4	30 min	3.0	Vulcanian
8/16/06–8/17/06					
Phases 1–2	11,750	0.4	3 h (broadband)	12	Vulcanian

classification is traditionally dependent on geological field survey measurements of tephra deposits. The most common measurements used to distinguish between eruption types are ash dispersal area (D) and the degree of fragmentation ($F\%$) (Walker, 1973) (Fig. 9). In order to determine these parameters field campaigns are necessary, which are both expensive and dangerous due to the location and activity of many volcanoes. In this section we attempt to make the most accurate classification of the four main eruptions at Tungurahua using geophysical observations obtained from the satellite, hand-held thermal, and infrasound data. Plume heights and dimensions as well as eruption duration and peak acoustic power are used to classify the eruptions (Table 5). Plume heights have been used for decades to

classify eruption types (Fig. 9a). Generally, the higher the eruption cloud reaches the more intense the eruption. Combining eruption intensity with duration allows for the magnitude of the eruption to be estimated. Plume dimension ratios of width to height can also aid in classifying the eruptions. A large umbrella cloud that spreads radially from the source will have a ratio of one, while a long and narrow plume will have a ratio closer to zero. A ratio of plume width to length close to one indicates that the eruption intensity was large enough to form an umbrella cloud that reached its neutral buoyancy level, acting as an expanding gravity current (Fig. 10). This means that the plume was strong enough to expand in all directions, including upwind. It should be noted that a plume ratio of one can also develop for low

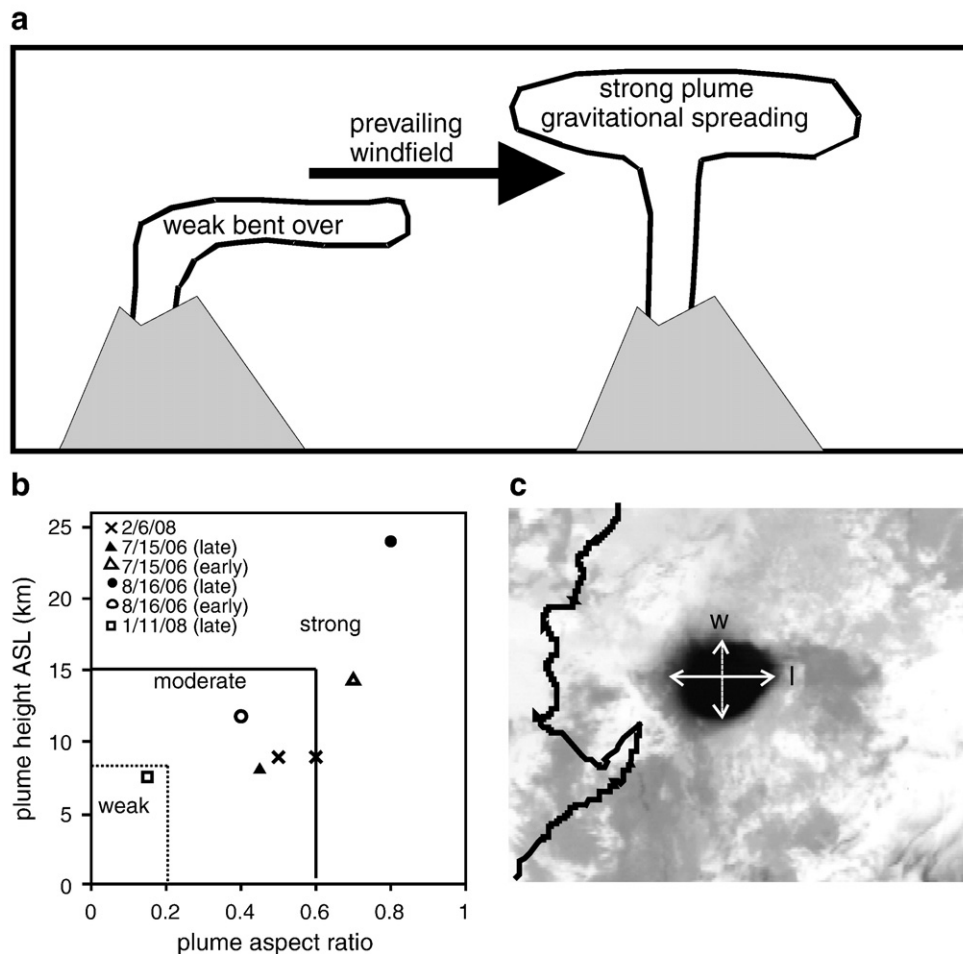


Fig. 10. Schematic depicting how plume ratios are determined. a – The different types of plume's that can result from the intensity of the eruption and strength of wind fields, adapted from Sparks et al., 1997. b – Plume ratios versus plume heights are calculated for the eruptions at Tungurahua. Plumes with a higher ratio are more energetic while those with lower ratios are less. c – An example of how plume ratios are determined from satellite imagery.

intensity plumes, but only if there are minimal winds, which is much less likely and did not occur during this study period. Eruption duration has also been used to determine eruption magnitude (the longer the eruption occurs the greater the total volume of erupted material). To that extent, acoustic power can also be related to the momentum transfer and therefore the higher the power, the more intense the eruption. These criteria will help us distinguish the different styles of eruptions that have occurred as well as observed transitions in eruption styles.

Although in this paper we only use peak acoustic power as a comparison variable to maximum height, the total acoustic energy for the duration of an eruption should also be used in estimates of eruption intensity. However, this would require a finer classification of acoustic event selection criteria, a challenging task which goes beyond the scope of this manuscript.

5.1. January 10th–11th 2008

The January eruptions are characterized by continuous low-level plumes reaching maximum heights of 7500 m. There was no identified jetting during the eruption sequence and the maximum infrasonic power levels reached were 4.3×10^4 W, with much variability throughout. The plume ratio ranged between 0.06 and 0.15 indicating it was a classic weak bent-over plume that was completely driven by wind fields and had no gravitational spreading (Sparks et al., 1997) (Fig. 10). Although many explosions were present throughout the eruption sequence, indicating typical strombolian activity (Fee et al., *in press*), the fact that there was a continuous plume suggests there was also sustained activity. With all the data collected it was determined that this eruption was the lowest intensity eruption that was investigated in this study, although it is difficult to precisely classify the type of eruptions. From the eruption plume height, the low acoustic power and low plume ratio the eruption can be constrained between intense strombolian activity or low-level vulcanian activity (Fig. 9b). The peak acoustic power estimate for this case is representative of impulsive transient events, in contrast to the later events which were more strongly dominated by jetting noise.

5.2. February 6th 2008

The February 6th 2008 eruption is characterized by several small eruption pulses followed by a higher intensity pulse. A total of four different phases can be distinguished by the satellite data with plume heights reaching a maximum height of 14,000 m. The total duration of the eruption was ~10.25 h, but within that time frame there were many fluctuations in acoustic intensity and periods of jetting that last no longer than 1.5 h at any time. These eruptions may be classified as typical vulcanian eruptions produced by a combination of jetting and discrete transient explosions, sending ash plumes to moderate altitudes (9000–14,000 m) (Fig. 9) (Sparks et al., 1997; Morrissey and Mastin, 2000; Parfitt and Wilson, 2008).

5.3. July 14th–15th 2006

The July eruption is characterized by a high intensity eruption with an emergent onset followed by a gradual decrease in eruption intensity. The plume reached a maximum height of 14,250 m during the first phase of the eruption, with maximum acoustic power of 9.8 MW. Infrasonic jetting occurred for 5 h, almost the entire duration of the first phase, although differences in the spectra are observed within the eruption duration (Fee et al., *in press*). Long eruption durations at high power are representative of high volume fluxes, and should be incorporated into more advanced eruption intensity classification schemas. Plume dimension ratios were determined using both the GOES and MODIS imagery and ranged between 0.8 and 0.74 during the first phase of the eruption indicating that there was a period when

gravitational settling was at least a partial driving force behind the plumes dispersal. When gravitational spreading is observed in eruption plume it means that the rising eruption column had enough momentum to attain its neutral buoyancy level, or above, before the wind field overpowers the column. This period was short-lived and the plume was advected by the wind fields which dispersed the plume to the southwest (Fig. 4). This earlier, more energetic portion of the plume can be classified as sub-plinian, as determined by the plume heights, the acoustic power, and the duration of the eruption. The plume reached high altitudes and had a prolonged period of jetting, but there was no stratospheric injection characteristic of plinian eruptions.

There was a decrease in activity at approximately 03:00 on July 15th, when the infrasonic jetting decreased and a lower intensity plume is observed still attached to the vent. This plume has much lower heights of 8000 m and a lower plume ratio of 0.4 (note this is an estimate, since the leading edge of the plume is not distinguishable). The maximum acoustic power during this phase was also much lower than the previous sequence at 3 MW with periods of variability. It was also observed in the hand-held thermal imagery that the plume was not being fed by a sustained column, but instead that there was column collapse and for the later portion small frequent dome collapses feeding sporadic pyroclastic flows. Therefore the plumes observed in the satellite imagery are likely PDCs or plumes supplied by PDCs. We have therefore determined that the sub-plinian eruption transitioned into a vulcanian eruption at approximately 03:15 (Fig. 9).

5.4. August 16th–17th 2006

The August eruption is characterized by a gradual increase followed by an emergent increase in eruption intensity. The maximum plume heights during the first, lower intensity, portion of the eruption were 11,750 m with maximum acoustic power reaching 12 MW. Broadband jetting was observed for the latter part of the first phase and lasted for ~1.5 h. The maximum plume ratio during this portion of the eruption was 0.4 indicating that gravitational forces were minimal. During this phase pyroclastic density currents were occurring frequently, possibly supplying a convective plume. From the maximum plume heights and the presence of uninterrupted broadband jetting for over an hour, we classify this portion of the eruption as vulcanian (Fig. 9). This eruption then transitioned into a more energetic eruption when a 24,000 m high umbrella cloud was injected into the stratosphere. The maximum acoustic power recorded for the eruption was over 50 MW. During this time pyroclastic density currents were also observed and were possibly feeding a larger convective plume that was being dispersed at a maximum height of 14,250 m. The plume ratios at this time were 0.8 indicating a strong gravitationally driven component of the plume. The gravitational spreading lasted for ~2 h. Since the eruption resulted in stratospheric injection of the eruption plume without the addition of external water, the radiation of intense, continuous broadband, very long period (VLP) infrasonic jetting for several hours, and the simultaneous emplacement of PDCs, this eruption can be classified as plinian (Sparks et al., 1997; Cioni et al., 2000; Parfitt and Wilson, 2008).

6. Conclusions

Four eruptions with varying eruption intensity were detected with satellite, thermal imaging and infrasound technologies and documented over a two-year period at Tungurahua Volcano. Transitions to and from different types of explosive activity were also characterized. Although both satellite data and infrasound data are useful tools for volcano monitoring, both techniques have limitations. Satellite data has become an established tool for estimating plume heights and tracking the dispersal of volcanic clouds and aerosols, but cannot detect activity during cloudy conditions, may have plume height uncertainties, and have difficulty constraining eruption onsets (if the

plume is too small to be detected in satellite imagery) and durations, especially during large eruptions where the volcanic clouds are obscuring the vent. Infrasound data, on the other hand, can easily detect the onset and end of eruptions as well as calculate relative power being produced by the eruptions in near real time. However, it has yet to be determined how the acoustic data can be robustly scaled to constrain plume heights or where the resulting ash and pyroclastic density currents are traveling, one of the most useful products for volcano hazard management. Therefore integrating the two techniques allows one to better constrain the eruption intensity, onset, cessation, and plume height. Combining the two datasets enables one to readily identify and characterize powerful eruptions (plinian, subplinian and intense vulcanian activity), but perhaps a different approach must be used to distinguish between lower intensity explosive eruptions (weak vulcanian and strombolian) (Fig. 9). Ongoing studies incorporating the two techniques will hopefully improve operational monitoring and hazard management for explosive eruptions.

Acknowledgements

The authors would like to take this opportunity to thank those who aided in the research and preparation of the manuscript. Thanks to Patricio Ramon and the Instituto Geofísico – Escuela Politécnica Nacional for providing the thermal imagery and other assistance, and Grace Swanson and Davida Streett of the Washington VAAC for sharing information about the ash monitoring and information gathered during the Tungurahua eruptions. In addition they would like to acknowledge Doug Drob of the NRL for the atmospheric G2S profiles, The NRL satellite application group for access to GOES data and the Goddard LAADS for MODIS data. This manuscript has been greatly improved by careful reviews by Ken Dean and Courtney Kearney. This work was made possible by the National Oceanic and Atmospheric Administration through the University of Mississippi subcontract 09-09022.

References

- Arellano, S.R., et al., 2008. Degassing patterns of Tungurahua volcano (Ecuador) during the 1999–2006 eruptive period, inferred from remote spectroscopic measurements of SO₂ emissions. *Journal of Volcanology and Geothermal Research* 176, 151–162.
- Barba, D., et al., 2006. Cronología de los Eventos Eruptivos de Julio y Agosto del 2006 del Volcan Tungurahua. Resúmenes extendidos de las 6th Jornadas en Ciencias de la Tierra, EPN_DG, Quito – Ecuador, pp. 177–180.
- Branney, M.J., Kokelaar, P., 2003. The origin, nature and behaviour of pyroclastic density currents, pyroclastic density currents and the sedimentation of ignimbrites. *Geological Society London, Memoir* 7–20.
- Bulletin of Global Volcanism Network (BGVN), 2008. Tungurahua. Smithsonian Institution. *Bulletin of Global Volcanism Network* 33 (06).
- Cansi, Y., 1995. An automatic seismic event processing for detection and location; the P.M.C.C. method. *Geophysical Research Letters* 22 (9), 1021–1024.
- Cas, R.A.F., Wright, J.V., 1988. *Volcanic Successions – Modern and Ancient*. Unwin Hyman, London. 528 pp.
- Casadevall, T.J., Krohn, M.D., 1995. Effects of the 1992 Crater Peak eruption on airports and aviation operations in the United States and Canada. *U.S. Geological Survey Bulletin* 2139.
- Casadevall, T.J., Matson, M., Riehle, J.R., 1992. Volcanic hazards and aviation safety – minimizing the threat through improved communications. *EOS Transactions, American Geophysical Union* 73 (43), 68.
- Cioni, R., Marianelli, P., Santacroce, R., Sbrana, A., 2000. Plinian and subplinian eruptions. In: Sigurdsson, R. (Ed.), *Encyclopedia of Volcanoes*. Academic Press, San Diego, CA, pp. 571–706.
- Dean, K.G., et al., 2004. Integrated satellite observations of the 2001 eruption of Mt. Cleveland, Alaska. *Journal of Volcanology and Geothermal Research* 127 (1–2), 87–105.
- Drob, D.P., Picone, J.M., Garces, M.A., 2003. Global morphology of infrasound propagation. *Journal of Geophysical Research* 108 (D21).
- Fee, D., Garces, M.A. and Steffke, A., in press. Infrasound from Tungurahua Volcano 2006–2008: Strombolian to Plinian Eruptive Activity. *Journal of Volcanology and Geothermal Research*. doi:10.1016/j.jvolgeores.2010.03.006.
- Garces, M.A., et al., 2008. Capturing acoustic fingerprint of stratospheric ash injection. *EOS Transactions* 89 (40), 377–378.
- Glaze, L.S., Francis, P.W., Self, S., Rothery, D.A., 1989. The 16 September 1986 eruption of Lascar volcano, north Chile: satellite investigations. *Bulletin of Volcanology* 51, 14911–14923.
- Hall, M., Robin, C., Beate, B., Mothes, P., Monzier, M., 1999. Tungurahua Volcano, Ecuador: structure, eruptive history, and hazards. *Journal of Volcanology and Geothermal Research* 91 (1), 1–21.
- Holasek, R.E., Self, S., 1995. GOES weather satellite observations and measurements of the May 18, 1980, Mount St. Helens eruption. *Journal of Geophysical Research* 100 (B5), 8469–8487.
- Holasek, R.E., Self, S., Woods, A.W., 1996a. Satellite observations and interpretation of the 1991 Mount Pinatubo eruption plumes. *Journal of Geophysical Research* 101 (B12), 27635–27655.
- Holasek, R.E., Woods, A.W., Self, S., 1996b. Experiments on gas-ash separation processes in volcanic umbrella plumes. *Journal of Volcanology and Geothermal Research* 70, 169–181.
- Johnson, J.B., 2003. Generation and propagation of infrasonic airwaves from volcanic explosions. *Journal of Volcanology and Geothermal Research* 121 (1–2), 1–14.
- Kienle, J., Shaw, G.E., 1979. Plume dynamics, thermal energy and long-distance transport of vulcanian eruption clouds from Augustine Volcano, Alaska. *Journal of Volcanology and Geothermal Research* 6, 139–164.
- Krueger, A.F., 1982. Geostationary satellite observations of the April 1979 Soufriere eruptions. *Science* 216, 1108–1109.
- Matoza, R.S., Fee, D., Garces, M.A., Seiner, J.M., Ramon, P.A., Hedlin, M.A.H., 2009. Infrasonic jet noise from volcanic eruptions. *Geophysical Research Letters* 36 (L08303).
- Matson, M., 1984. The 1982 El Chichon volcano eruption – a satellite perspective. *Journal of Volcanology and Geothermal Research* 23, 1–10.
- Miller, T.P., Chouet, B.A., 1994. Preface. *Journal of Volcanology and Geothermal Research* 62 (1–4) vii–vii.
- Morrissey, M.M., Mastin, L.G., 2000. Vulcanian eruptions. In: Sigurdsson, R. (Ed.), *Encyclopedia of Volcanoes*. Academic Press, San Diego, CA, pp. 463–475.
- Parfitt, E., Wilson, L., 2008. *Fundamentals of Physical Volcanology*, 230. Blackwell Publishing, Oxford.
- Robock, A., Matson, M., 1983. Circumglobal transport of the El Chichon Volcanic Dust Cloud. *Science* 221, 195–197.
- Rose, W.I., Kostinski, A.B., Kelley, L., 1995. Real-time C-band radar observations of 1992 eruption clouds from Crater Peak, Mount Spurr Volcano, Alaska. *U.S. Geological Survey Bulletin* B2139.
- Schneider, D.J., Rose, W.I., 1994. Observations of the 1989–90 Redoubt Volcano eruption clouds using AVHRR satellite imagery. In: Casadevall, T.J. (Ed.), *Volcanic Ash and Aviation Safety: Proceedings of the First International Symposium on Volcanic Ash and Aviation Safety*. U.S. Geological Survey Bulletin B, 2047, pp. 405–418.
- Schneider, D.J., et al., 1999. Early evolution of a stratospheric volcanic eruption cloud as observed with TOMS and AVHRR. *Journal of Geophysical Research* 104 (D4), 4037–4050.
- Sparks, R.S.J., Wilson, L., Hulme, G., 1978. Theoretical modeling of the generation, movement, and emplacement of pyroclastic flows by column collapse. *Journal of Geophysical Research* 83 (B4), 1727–1739.
- Sparks, S.J., Moore, J.G., Rice, C.J., 1986. The initial giant umbrella cloud of the May 18th, 1980, explosive eruption of Mount St. Helens. *Journal of Volcanology and Geothermal Research* 28, 257–274.
- Sparks, R.S.J., et al., 1997. *Volcanic Plumes*. John Wiley & Sons, Chichester. 559 pp.
- Tupper, A., Oswalt, S.J., Rosenfeld, D., 2005. Satellite and radar analysis of the volcanic-cumulonimbus at Mount Pinatubo, Philippines, 1991. *Journal of Geophysical Research* 110 (D09204). doi:10.1029/2004JD005499.
- Walker, G.P.L., 1973. Explosive volcanic eruptions – a new classification scheme. *International Journal of Earth Science* 62 (2), 431–446.
- Watson, I.M., et al., 2004. Thermal infrared remote sensing of volcanic emissions using the Moderate Resolution Imaging Spectroradiometer (MODIS). *Journal of Volcanology and Geothermal Research* 135, 75–89.
- Wen, S., Rose, W.I., 1994. Retrieval of sizes and total masses of particles in volcanic clouds using AVHRR bands 4 and 5. *Journal of Geophysical Research* 99, 5421–5431.